



**HAL**  
open science

# Understanding the mechanisms behind the northward extension of the West African Monsoon during the Mid-Holocene

Marco Gaetani, Gabriele Messori, Qiong Zhang, Cyrille Flamant, Francesco S. R. Pausata

## ► To cite this version:

Marco Gaetani, Gabriele Messori, Qiong Zhang, Cyrille Flamant, Francesco S. R. Pausata. Understanding the mechanisms behind the northward extension of the West African Monsoon during the Mid-Holocene. *Journal of Climate*, 2017, 30 (19), pp.7621-7642. 10.1175/JCLI-D-16-0299.1 . insu-01545606

**HAL Id: insu-01545606**

**<https://insu.hal.science/insu-01545606>**

Submitted on 27 Jun 2017

**HAL** is a multi-disciplinary open access archive for the deposit and dissemination of scientific research documents, whether they are published or not. The documents may come from teaching and research institutions in France or abroad, or from public or private research centers.

L'archive ouverte pluridisciplinaire **HAL**, est destinée au dépôt et à la diffusion de documents scientifiques de niveau recherche, publiés ou non, émanant des établissements d'enseignement et de recherche français ou étrangers, des laboratoires publics ou privés.



# AMERICAN METEOROLOGICAL SOCIETY

*Journal of Climate*

## **EARLY ONLINE RELEASE**

This is a preliminary PDF of the author-produced manuscript that has been peer-reviewed and accepted for publication. Since it is being posted so soon after acceptance, it has not yet been copyedited, formatted, or processed by AMS Publications. This preliminary version of the manuscript may be downloaded, distributed, and cited, but please be aware that there will be visual differences and possibly some content differences between this version and the final published version.

The DOI for this manuscript is doi: 10.1175/JCLI-D-16-0299.1

The final published version of this manuscript will replace the preliminary version at the above DOI once it is available.

If you would like to cite this EOR in a separate work, please use the following full citation:

Gaetani, M., G. Messori, Q. Zhang, C. Flamant, and F. Pausata, 2017: Understanding the mechanisms behind the northward extension of the West African Monsoon during the Mid-Holocene. *J. Climate*. doi:10.1175/JCLI-D-16-0299.1, in press.

© 2017 American Meteorological Society



1 **Understanding the mechanisms behind the northward extension of the West African**  
2 **Monsoon during the Mid-Holocene**

3

4 Marco Gaetani (1), Gabriele Messori (2), Qiong Zhang (3), Cyrille Flamant (1), Francesco  
5 S.R. Pausata (2,4)

6

7 (1) LATMOS/IPSL, UPMC Univ. Paris 06 Sorbonne Universités, UVSQ, CNRS, Paris,  
8 France

9 (2) Department of Meteorology and Bolin Centre for Climate Research, Stockholm  
10 University, Stockholm, Sweden

11 (3) Department of Physical Geography and Bolin Centre for Climate Research, Stockholm  
12 University, Stockholm, Sweden

13 (4) Department of Earth and Atmospheric Sciences, University of Quebec in Montreal,  
14 Montreal (QC), Canada

15

16 Corresponding author: Marco Gaetani

17 Laboratoire Atmosphères, Milieux, Observations Spatiales, LATMOS-IPSL

18 Université Pierre et Marie Curie

19 Boite 102, Tour 45, 3eme Etage, Couloir 45-46

20 4 Place Jussieu, 75252 Paris Cedex 05, France

21 Tel: +33 1 44 27 48 72

22 e-mail: marco.gaetani@latmos.ipsl.fr

23 **Abstract**

24

25 Understanding the West African monsoon (WAM) dynamics in the mid-Holocene (MH) is a  
26 crucial issue in climate modelling, because numerical models typically fail to reproduce the  
27 extensive precipitation suggested by proxy evidence. This discrepancy may be largely due to  
28 the assumption of both unrealistic land surface cover and atmospheric aerosol concentration.  
29 In this study, the MH environment is simulated in numerical experiments by imposing  
30 extensive vegetation over the Sahara and the consequent reduction in airborne dust  
31 concentration. A dramatic increase in precipitation is simulated across the whole of West  
32 Africa, up to the Mediterranean coast. This precipitation response is in better agreement with  
33 proxy data, in comparison with the case in which only changes in orbital forcing are  
34 considered. Results show a substantial modification of the monsoonal circulation,  
35 characterized by an intensification of large-scale deep convection through the entire Sahara,  
36 and a weakening and northward shift ( $\sim 6.5^\circ$ ) of the African easterly jet. The greening of the  
37 Sahara also leads to a substantial reduction in African easterly wave activity and the  
38 associated precipitation. The reorganization of the regional atmospheric circulation is driven  
39 by the vegetation effect on radiative forcing and associated heat fluxes, with the reduction in  
40 dust concentration to enhance this response. The results for the WAM in the MH present  
41 important implications for understanding future climate scenarios in the region and in  
42 teleconnected areas, in the context of projected wetter conditions in West Africa.

43

44 **Key words:** African humid period, African easterly waves, dust, land cover, Green Sahara,  
45 EC-Earth

## 46 **1 Introduction**

47

48 Understanding climate variability in West Africa is one of the most challenging issues in  
49 current climate science, from both the academic and socio-economic perspectives. Indeed,  
50 food security in West African countries is largely based on rain fed agriculture [IFAD, 2013]  
51 and is potentially vulnerable to climate variability [Sultan and Gaetani, 2016]. Precipitation in  
52 West Africa is concentrated in the boreal summer and is primarily associated with the West  
53 African Monsoon (WAM) [Nicholson, 2013]. The WAM underwent large variability in the  
54 20th century, showing a succession of long lasting wet and dry periods following  
55 multidecadal trends [Rodríguez-Fonseca et al., 2015]. In this context, the need for reliable  
56 predictions of rainfall in West Africa on decadal and longer time scales is crucial. However,  
57 state-of-the-art climate models are still deficient in correctly reproducing the historical  
58 variability and agreeing on future projections [Biasutti, 2013]. The skill in identifying and  
59 disentangling the numerous drivers of the WAM variability that operate at different spatial  
60 and temporal scales is modest at best [Biasutti et al., 2009; Rowell, 2013].

61

62 Furthermore, climate change in West Africa has been much larger during the Holocene  
63 interglacial period than in the 20th century. Extreme droughts, developing in a matter of few  
64 years or decades, have been recorded during late Holocene (5-0 kyr BP), with dramatic lake  
65 low stands near the Equator [Shanahan et al., 2006] and the complete drying of fresh water  
66 bodies in the Sahel [Gasse, 2000]. The opposite scenario occurred during early Holocene,  
67 between 15 and 5 kyr ago, when increased summer precipitation led to an expansion of the  
68 North African lakes and wetlands and an extension of grassland and shrubland into areas that  
69 are now desert, giving origin to the so-called “Green Sahara”, or African Humid Period  
70 (AHP) [Holmes, 2008]. Model simulations for the mid-Holocene (MH, 6 kyr BP) show

71 limitations in reproducing the intensification and geographical expansion of the WAM  
72 precipitation [Harrison et al., 2014], and these shortcomings may be similar to those affecting  
73 historical simulations and future projections. In general, numerical simulations of the WAM  
74 dynamics are particularly sensitive to the shortcomings commonly affecting climate model  
75 physics, such as the inaccurate representation of clouds, energy fluxes, coupling at the  
76 surface, and convection at the sub-grid scale. Moreover, the coarse resolution of global  
77 climate models is insufficient to properly simulate the mesoscale convection characterizing  
78 the WAM precipitation. In historical simulations, fully coupled models exhibit biases in  
79 reproducing the tropical Atlantic dynamics, resulting in warmer SST and weaker monsoonal  
80 circulation [Roehrig et al., 2013]. In the description of future climate scenarios, the model  
81 sensitivity to the global surface warming, and to the direct CO<sub>2</sub> radiative forcing, appears  
82 crucial for the sign of the projected precipitation trends [Giannini, 2010; Gaetani et al.,  
83 2016].

84

85 A number of studies have addressed the limitations in modelling the West African climate in  
86 the MH, pointing to Saharan land cover as the key ingredient to simulate precipitation  
87 patterns fitting paleoclimate data. By using a coupled atmosphere-vegetation model, Claussen  
88 and Gayler [1997] found an amplification of the response of the atmospheric circulation to  
89 changes in the Earth's orbit produced by a positive precipitation-vegetation feedback. By  
90 prescribing a vegetated Sahara, several authors found a good agreement between simulated  
91 precipitation and paleoclimate data, and identified the increased low-level moisture, which  
92 destabilizes the vertical column and enhances convection, as a crucial factor to maintain the  
93 intensification of the monsoon system due to the orbital forcing [Su and Neelin, 2005;  
94 Patricola and Cook, 2007; Swann et al., 2014]. The use of interactive vegetation climate  
95 models confirms the positive precipitation-vegetation feedback and the key role of the latent

96 heat increase in favoring the convection [Patricola and Cook, 2008; Rachmayani et al., 2015],  
97 though the importance of the decrease in surface albedo is also highlighted [Levis et al.,  
98 2004]. A recent study has shown that accounting for the large reduction in airborne dust  
99 emission is also essential for an accurate simulation of the WAM strength during the MH  
100 [Pausata et al., 2016]. The authors pointed out that the Paleoclimate Modelling  
101 Intercomparison Project (PMIP) [Braconnot et al., 2011] and the Coupled Model  
102 Intercomparison Project (CMIP) [Taylor et al., 2012] protocols specify the MH dust  
103 concentration and land cover to be equal to the pre-industrial (PI) period, which may be the  
104 main cause of the models' dry bias in simulating the MH WAM. In recent numerical  
105 experiments, the inclusion of both dynamic vegetation and dust emissions is not sufficient to  
106 reproduce an intensification of the WAM compatible with paleoclimate data, if the initial  
107 configuration for the vegetation is set to PI levels. Indeed, the simulated precipitation changes  
108 do not allow vegetation to grow north of 15° N, and the associated variations in dust load  
109 compared to PI climate are limited, and so are the feedbacks [Harrison et al., 2015].

110

111 Building upon the study of Pausata et al. [2016], this work aims to describe in detail the  
112 dynamics of the WAM during the MH, elucidating the mechanisms whereby changes in land  
113 cover and associated mineral dust emission alter atmospheric circulation and precipitation  
114 patterns. For this purpose, fully coupled climate model experiments, in which Saharan  
115 vegetation and dust concentrations are changed concomitantly and in turn, are analyzed. In  
116 the context of the existing literature on the topic, the analysis of the mineral dust's role in  
117 modifying the atmospheric dynamics under vegetated Sahara conditions represents a novel  
118 and original contribution to the understanding of the WAM system in the MH. The results of  
119 this study are particularly relevant not only from a paleoclimate perspective but also with  
120 respect to the assessment of future scenarios for West Africa [Schmidt et al., 2014]. Indeed, a

121 number of projections simulate a positive precipitation trend, and a subsequent land greening  
122 and dust reduction [Evan et al., 2016]. The paper is organized as follows: the climate model  
123 and the experimental design are described in section 2, the results are presented and discussed  
124 in section 3, and the main findings are summarized in section 4.

125

## 126 **2 Model and experimental setup**

127

128 In the present study, the climate simulations performed by Pausata et al. [2016], using version  
129 3.1 of the atmosphere-ocean fully coupled climate model EC-Earth [Hazeleger et al., 2010],  
130 are analyzed. The atmospheric model is based on the Integrated Forecast System (IFS cycle  
131 36r4) [ECMWF, 2010], including the H-TESEL land model [van den Hurk et al., 2000]. In  
132 the land model, each grid-box is divided into fractions (bare ground, low and high vegetation,  
133 intercepted water, shaded and exposed snow are represented over land), with properties  
134 defining separate heat and water fluxes used in an energy balance equation solved for the skin  
135 temperature. A fraction of the rainfall is collected by an interception layer, where the  
136 remaining fraction is partitioned between surface runoff and infiltration. Infiltration and  
137 runoff schemes depend on the soil texture and standard deviation of orography. The  
138 simulation is run at T159 horizontal spectral resolution ( $\sim 1.125^\circ$ , approximately 125 km)  
139 with 62 vertical levels. The atmospheric component is coupled by the OASIS 3 coupler  
140 [Valcke, 2006] to the Nucleus for European Modelling of the Ocean version 2 (NEMO)  
141 [Madec, 2008], and the Louvain-la-Neuve Sea Ice Model version 3 (LIM3) [Vancoppenolle  
142 et al., 2008]. The ocean component NEMO has a nominal horizontal resolution of  $1^\circ$  and 46  
143 vertical levels.

144

145 A control simulation (CTL) is performed following the PMIP3 protocol [Braconnot et al.,  
146 2011]. The orbital forcing is set to MH values (6 kyr BP). For the greenhouse gases, the  
147 methane is set at 650 ppb, instead of the 760 ppb PI value, and CO<sub>2</sub> and other greenhouse  
148 gases are set to PI levels. Aerosol particle emissions, the solar constant, ice sheets,  
149 topography and coastlines are set to PI conditions. The CTL run is compared to three  
150 sensitivity experiments, which simulate the MH climate in the presence of a Green Sahara  
151 with reduced atmospheric dust concentrations (GSRD), a Green Sahara with PI dust (GSPD),  
152 and a present-day Sahara with reduced dust (PSRD).

153

154 The changes in vegetation in the GSRD and GSPD experiments are imposed by prescribing the  
155 vegetation type over the Sahara-Sahel region [11°-33°N, 15°W-35°E] to be evergreen shrub  
156 with a leaf area index (LAI) equal to 2.6. The change in vegetation cover leads to a decrease in  
157 the albedo (averaged into the Sahara-Sahel region) from 0.30 to 0.15 (Table 1). Surface  
158 roughness and soil wetness are prescribed to PI values in the sensitivity experiments. As  
159 discussed in detail in Pausata et al. [2016], the experiment design is idealized. Nevertheless,  
160 recent studies have shown that paleolakes extended at least to 28°N [Lézine et al., 2011] and  
161 tropical vegetation migrated as far as 24°N during the AHP, about 1000 km further north than  
162 today [Hély et al., 2014]. Based on leaf wax isotopes, Tierney et al. [2017] show that the Green  
163 Sahara extended all the way to the northern most part of western Sahara, with peaks in  
164 precipitation above 1000 mm/year relative to present day. Hence, proxy evidence suggests an  
165 extensive greening across the entire Sahara during the MH, overall supporting the choice of  
166 the prescribed vegetation cover in the GSRD and GSPD experiments. Furthermore, Pausata et  
167 al. [2016] have shown that changes in WAM strength do not strongly depend on the exact  
168 choice of the vegetation type prescribed over eastern Sahara, which may have experienced  
169 dryer conditions compared to the western part.

170

171 The atmospheric dust concentration is prescribed in the CTL simulation by using the PI dust  
172 climatology derived from the Community Atmosphere Model [Albani et al., 2014], which is  
173 used in the CMIP5 exercise. The size distribution of dust corresponds to diameter ranges  
174 from 0.1 to 10.0  $\mu\text{m}$ . The model used in this study simulates the direct effect of dust on the  
175 atmospheric radiative balance, while the indirect effect on cloud formation and microphysics  
176 is not included. To take into account the decreased dust emission and concentration typical of  
177 the AHP, in the GSRD and PSRD experiments the PI dust concentration is reduced by 80%  
178 throughout the troposphere (up to 150 hPa) over a broad area around the Sahara desert (see  
179 Figure S1 in Pausata et al. [2016]). This choice is justified by evidence from proxy records  
180 off the coast of Morocco showing a dust flux reduction of 60-80% [deMenocal et al., 2000;  
181 McGee et al., 2013], and also supported by a recent dust modelling study [Egerer et al.,  
182 2016]. The imposed dust reduction leads to a decrease in the global dust aerosol optical depth  
183 (AOD) of almost 60% and in the total AOD of 0.02 (see Figure 1 in Pausata et al. [2016]).  
184 The PI climatological dust mixing ratio prescribed in the CTL and GSPD simulations (Figure  
185 1a) closely represents the main features of the present-day dust distribution over North  
186 Africa, namely the peak over the Bodélé depression north of Lake Chad, and the band over  
187 western Sahara and Sahel [Ginoux et al., 2012]. An intense peak in concentration is present  
188 over eastern Sahara, largely dominating the African dust emission in summer, which appears  
189 as an artifact when compared with satellite retrievals for the present-day distribution  
190 (compare Figure 1a with Figure 4 in Ginoux et al. [2012]). This artifact affects the radiative  
191 balance simulated in the region, by masking the dust sources to the west, with potential  
192 repercussions on the simulation of the regional atmospheric dynamics. Additional simulations  
193 have been performed to test the effect of imposing a more realistic dust climatology, finding  
194 barely significant differences in the effect of dust reduction on precipitation (see Figures S1-

195 S3 in the Supplementary Material online). However, dust emission from the central and  
196 western Sahara is intimately linked to the surface wind pattern over North Africa, which  
197 shows a broad variability at multidecadal time scales [Evan et al., 2016]. Thus, substantial  
198 differences in the surface wind fields in the PI period could explain this apparently  
199 incongruous dust concentration pattern produced by the CAM model. However, the  
200 meridional profile of dust concentration (averaged between 15°W and 25°E, to cut the  
201 unusual peak to the east off) is close to the present-day pattern, showing a dust layer reaching  
202 the mid-troposphere, with an intense peak around 15-20°N (corresponding to the Bodélé and  
203 western Sahara sources), and a mid-tropospheric plume extending south to the Gulf of Guinea  
204 (Figures 1c, e). When the dust concentration is reduced by 80%, the highest anomalies are  
205 located where the PI concentration is maximum, namely over central and eastern Sahara,  
206 around 15-20°N, up to 800-700 hPa (Figures 1b, d, f).

207

208 In each experiment, initial conditions are taken from a 700-year PI spin-up run, and the  
209 simulations are then run for about 300 years. The quasi-equilibrium is reached after 100-200  
210 years depending on the experiment. This study focuses on the monsoonal season (June to  
211 September, JJAS) for the last 30 years of each experiment. The experimental setup is  
212 summarized in Table 1, and a detailed description is presented in Pausata et al. [2016], along  
213 with a more comprehensive discussion of the model's performances.

214

### 215 **3 Results**

216

217 This section presents the impacts of changes in Saharan vegetation and dust concentration on  
218 precipitation and atmospheric dynamics over West Africa in each sensitivity experiment  
219 relative to the MH reference simulation (CTL). The responses in the radiative and energy

220 variables are then analyzed. Unless otherwise specified, the significance of the changes is  
221 estimated via a two-tailed Student's t-test at the 95% confidence level.

222

### 223 **3.1 Precipitation and Dynamics**

224

225 In the CTL simulation (Figure 2a), the climatological WAM precipitation is consistent with  
226 the “classical” pattern observed in the PI and historical periods [Nicholson, 2013]. The peak  
227 precipitation reaches over 16 mm/day on the western coastline around 10°N, and  
228 approximately 10 mm/day in the interior, slightly in excess of present-day observations (not  
229 shown), but in agreement with the most CMIP5 models [Harrison et al., 2014]. The  
230 northernmost extent of the monsoon is just above 16°N, 2° latitude further north than a PI  
231 simulation performed using the same model (see Figure S6 in Pausata et al. [2016]). The  
232 main change in the precipitation pattern in the GSRD experiment is a dramatic increase of  
233 precipitation over the whole North African subcontinent, with significant anomalies spanning  
234 10°N to 25°N and extending to the Mediterranean coast in the western sector (Figures 2b, c).  
235 The response in the GSPD experiment (Figures 2d, e) is qualitatively similar to the GSRD  
236 experiment, though slightly weaker in intensity and extension, suggesting that the dust  
237 reduction tends to enhance the vegetation forcing (see the GSRD-GSPD difference in Figure  
238 2h). In the Green Sahara experiments, the location of the precipitation maximum is around  
239 15°N (Figure 2b, d), consistently with the proxy-based estimation by Hély et al. [2014]. The  
240 simulated yearly precipitation anomalies exceed 700 mm around the peak (10°-20°N), and  
241 reach 300 mm in the Sahara region (20°-30°N). Skinner and Poulsen [2016] find similar  
242 precipitation anomalies extending into the late monsoonal season, pointing out the role of  
243 extratropical troughs advecting tropical moisture toward the Sahara in the form of  
244 concentrated plumes of water vapor. These values are in line with MH precipitation

245 reconstructions based on diverse paleoclimate proxies, which estimate the difference with the  
246 present day over West Africa in the range 300-500 mm [Kröpelin et al., 2008; Harrison et al.,  
247 2014; Tierney et al., 2017]. On the other hand, the reduction of dust alone in the PSRD  
248 experiment leads to reduced precipitation over the Sahelian belt relative to the CTL case  
249 (Figures 2f, g).

250

251 The wind pattern at 925 hPa in the CTL simulation is dominated by the southwesterly moist  
252 monsoonal flow from the Tropical Atlantic, the northeasterly Harmattan dry wind, and the  
253 cyclonic gyre associated with the Saharan Heat Low (SHL, [Lavaysse et al., 2009]), located  
254 around [10°W-10°E, 20°-30°N] (Figure 3a). In the GSRD experiment (Figure 3b), the mean  
255 wind pattern displays a general northward shift, relative to the MH CTL simulation, resulting  
256 in an intensification of the monsoonal flow and a weakening of the Harmattan wind and the  
257 SHL (-2.1 K at the peak). The latter migrates 3.2° to the north (Figure 3c), coherently with  
258 the precipitation response shown in Figures 2b, c. In comparison to the GSRD experiment,  
259 the GSPD experiment shows a similar response in the wind field (Figure 3h), with a slightly  
260 stronger SHL (+0.9 K at the peak), displaced 0.7° to the south (Figure 3d, e). The negative  
261 precipitation response in the Sahel simulated in the PSRD experiment (Figures 2f, g) is  
262 instead associated with a weakening of the monsoonal flow and a deeper southward  
263 penetration of the Harmattan in the eastern Sahel, accompanied by a 0.7° southward  
264 migration of the SHL (Figures 3f, g).

265

266 In the CTL simulation, the mid-tropospheric (700 hPa) wind field appears similar, in its main  
267 features, to the circulation pattern characterizing the present-day WAM (Figure 4a). The  
268 African Easterly Jet (AEJ) axis is located around 16°N, and the anticyclonic gyre of the  
269 Saharan high contrasts the SHL in the lower troposphere [Chen, 2005]. The GSRD

270 experiment shows a dramatic reorganization of the circulation, with a significant 6.5°  
271 northward shift and 2.7 m/s weakening of the AEJ, and the installation of a westerly flow  
272 around 10-15°N. This results in a large-scale cyclonic gyre over West Africa around 15°N,  
273 and a substantial weakening of the Saharan high (Figures 4b, c). The wind field response in  
274 the GSPD experiment shows a similar structure in comparison with the GSRD experiment,  
275 but in this case the Saharan high is slightly stronger and the AEJ is slightly weaker and  
276 displaced 1.2° to the south (Figures 4d, e, h). In present-day atmospheric dynamics, the AEJ  
277 is maintained by the soil moisture gradient at the surface and the two meridional circulations  
278 forced by the dry convection of the SHL to the north and the moist convection associated  
279 with the intertropical convergence zone (ITCZ) to the south [Thorncroft and Blackburn 1999;  
280 Wu et al. 2009]. Therefore, the weakening and northward shift of the jet in the Green Sahara  
281 scenario is the expected response to the vanished surface soil moisture gradient and the  
282 substantial reduction of the SHL-associated circulation. In the PSRD experiment, the only  
283 significant change is a 1.5° southward shift of the AEJ compared to the CTL (Figures 4f, g).  
284 Very similar response patterns are observed at 500 hPa (Figure S4), pointing to the  
285 emergence of an intense westerly flow around 10°N from low levels up to the mid-  
286 troposphere, and a remarkable limitation in the southward extension of the Saharan high in  
287 the GSRD and GSPD experiments.

288

289 The upper tropospheric circulation at 200 hPa is dominated by the Tropical Easterly Jet (TEJ)  
290 axis between 0 and 15°N over Africa, the subtropical jet from the Mediterranean Sea to mid-  
291 latitudes in western Asia, and the subpolar jet at mid-latitudes over the North Atlantic (Figure  
292 5a). The GSRD and GSPD experiments (Figures 5b-e) show a general intensification of the  
293 zonal circulation in the upper troposphere, characterized by a northward shift of the  
294 subtropical jet and the emergence of an easterly jet streak around 15°N over West Africa. The

295 responses in GSRD and GSPD are not significantly different (Figures 5c, e, h). The response  
296 of the zonal circulation in the upper troposphere to the greening of the Sahara is interpreted as  
297 the upper branch of an anomalous Walker-like circulation (Figure S5), generated by the  
298 widespread intensification of deep convection, and connected with the strengthened westerly  
299 flow in the lower troposphere (see Figures 3c, e). In the PSRD experiment, the zonal  
300 circulation is weakened and shifted slightly southward (Figures 5f, g).

301

302 The dramatic reorganization of the regional circulation in the GSRD experiment is also  
303 revealed by the meridional overturning circulation averaged over West Africa [10°W, 10°E]  
304 (Figure 6). The CTL experiment simulates a circulation pattern resembling the large scale  
305 dynamics associated with the present-day WAM (Figure 6a): (i) the southern hemisphere  
306 Hadley cell, (ii) the southerly monsoonal flow in the lower troposphere reaching the Sahel,  
307 (iii) the deep convection associated with the ITCZ, (iv) the dry shallow convection over the  
308 Sahara associated with the SHL, contrasting with the subsidence associated with the Saharan  
309 high in the mid-troposphere (500-600 hPa) [Nicholson, 2013]. In the GSRD and GSPD  
310 experiments, the change in surface conditions over the Sahara leads to an extension of the  
311 deep convection up to 30-35°N, which cancels the mid-tropospheric divergence associated  
312 with the SHL shallow convection contrasting the Saharan high subsidence (Figures 6b, d).  
313 The reduction in dust concentration amplifies the response to the land cover change, inducing  
314 stronger anomalies in deep convection over the Sahel and the Sahara desert (Figures 6c, e, h).  
315 The PSRD experiment does not show any substantial systematic changes in the atmospheric  
316 meridional overturning circulation compared to the CTL experiment (Figure 6f, g).

317

318 The analysis discussed above shows that a greening of the Sahara has a dramatic impact on  
319 West African precipitation, introducing unusual features in the monsoon-related regional

320 circulation. Summarizing, rainfall intensifies over the Sahara and extends all the way up to  
321 the Mediterranean coast (Figure 2), and some of the dynamical features characterizing the  
322 “classical” WAM picture are substantially altered. The monsoonal flow extends far to the  
323 north and into the mid-troposphere, weakening the AEJ and shifting it northward by 6.5°  
324 (Figures 3 and 4). Moreover, the mid-tropospheric contrast between the SHL convection and  
325 the Saharan high subsidence vanishes (Figures 3 and 4). These changes appear as a general  
326 reorganization of the circulation towards a cyclonic gyre throughout the troposphere,  
327 resulting from the development of deep convection over the Sahara (Figure 6). Patricola and  
328 Cook [2007] described similar modifications to the monsoonal dynamics during the MH, by  
329 prescribing shrubland north of approximately 20° in regional climate model simulations. The  
330 present study highlights that the reduction in dust concentration, following the greening of the  
331 Sahara, amplifies the impact of land cover change. On the other hand, the effect of reduction  
332 in dust alone results in a weak decrease in the Sahelian precipitation, accompanied by small  
333 changes in the atmospheric circulation. This suggests a peculiar role of dust reduction in  
334 amplifying the anomalies when associated with land cover changes.

335

336 The changes in the WAM atmospheric dynamics are accompanied by important changes in  
337 the mechanisms driving the precipitation. A major source of synoptic-scale rainfall variability  
338 throughout present-day West Africa is associated with the African easterly waves (AEWs):  
339 westward propagating disturbances with wavelengths of approximately 3000 km and periods  
340 below 5-6 days [Diedhiou et al., 1998]. A longer-period regime of 6-9 day waves has also  
341 been identified in the region [Diedhiou et al., 1998; 1999], but these typically display a  
342 weaker association with precipitation [Gu et al., 2004]. The AEWs are particularly important  
343 over the Sahel, where they modulate rainfall through the initiation and organization of  
344 mesoscale convective systems (MCSs) and squall lines during the monsoonal season [Skinner

345 and Diffenbaugh, 2013]. AEW activity is detected in each experiment by computing the  
346 variance of the daily meridional wind at 700 hPa, after the application of a 2.5-5 day  
347 bandpass filter. As in Diedhiou et al. [1998, 1999] and Gu et al. [2004], “wavy” days are  
348 defined here as the days where the filtered southerly wind is at maximum and exceeds 0.5  
349 m/s at a reference point. Such point is chosen to be representative of the main track of wave  
350 activity as defined by the filtered meridional wind in the different simulations. For the CTL  
351 and PSRD cases, the location [15°N, 0°E] is selected, similarly to studies analyzing the  
352 present-day monsoon (e.g. Diedhiou et al., [1999]). For the GSPD and GSRD simulations,  
353 the location [20°N, 0°E] is selected, reflecting the significant northward shift of the  
354 monsoonal circulation. It is noted that the results are relatively insensitive to small meridional  
355 shifts in the reference point (not shown, see also Gu et al., [2004]). The precipitation is then  
356 averaged over the selected days and the JJAS climatology for each experiment is subtracted,  
357 in order to calculate the precipitation anomalies associated with wavy days in mm/day. As a  
358 caveat, it is noted that this methodology implicitly assumes that all the precipitation occurring  
359 during a wavy day can be ascribed to MCSs associated to AEWs.

360

361 The CTL simulation displays a band of wave activity that originates west of the Ethiopian  
362 highlands and maximizes over western Sahel, propagating across the Tropical Atlantic Ocean  
363 (Figure 7a). This is similar to what seen in reanalysis data, albeit with larger variance values  
364 (see Figure 3 in Skinner and Diffenbaugh [2013]). Both the GSRD and GSPD experiments  
365 (Figures 7b-e) show a northward shift and a marked weakening of the meridional wind  
366 variance in the region affected by the AEW activity. The difference between GSRD and  
367 GSPD indicates that the dust reduction favors a further weakening of the AEW activity in the  
368 presence of a vegetated Sahara (Figure 7h). Conversely, the PSRD experiment presents a  
369 weakened AEW pattern relative to the CTL simulation (Figures 7e, f).

370

371 Since the definition of a wavy day focuses on meridional wind maxima, their frequency is  
372 similar across all simulations, ranging from 25.5% in the CTL simulation to 24.0% in the  
373 PSRD case. However, the intensity of these AEW episodes shows a broader spread, with the  
374 CTL simulation displaying a mean filtered meridional wind velocity of 2.6 m/s compared to  
375 the 2.3 m/s of the GSPD case and the 2.1 m/s of the GSRD case. A one-sided two-sampled  
376 Kolmogorov-Smirnov test confirms that the cumulative distribution function of the AEW  
377 intensity for the GSPD case is larger than that of the CTL at the 95% confidence level,  
378 indicating a shift of the distribution towards lower values.

379

380 The significant differences in the filtered meridional wind variance and AEW intensity result  
381 in equally large changes in the precipitation associated with the AEWs. The precipitation on  
382 wavy days is characterized by a multipolar anomaly pattern, clearly showing the signature of  
383 a propagating wave (Figure 8). The peak precipitation anomalies driven by the AEW-  
384 associated MCSs are not co-located with the reference points at which the waves are  
385 identified. Rather, the peaks tend to occur to the west or south-west of the reference points, in  
386 close agreement with previous studies (e.g., Diedhiou et al. [1999] and Gu et al. [2004]). The  
387 peak average precipitation anomaly in the CTL simulation is 4.7 mm/day (Figure 8a), and  
388 wavy days account for 41.5% of the total seasonal precipitation at that location (Figure 8b).  
389 The GSPD and GSRD simulations display a clear northward shift of the dipole, with a sizable  
390 reduction of the average peak precipitation anomalies on wavy days to 1.6 and 2.3 mm/day,  
391 respectively (Figures 8c, e). These correspond to 36.5% and 33.3% of the total precipitation  
392 (Figures 8d, f), respectively. The dust reduction alone leads to slight changes in this pattern,  
393 with a 4.1 mm/day peak anomaly, representing 39.2% of the total precipitation.

394

395 The decreased importance of AEWs under Green Sahara conditions indicates a shift towards  
396 variability on time scales longer than the synoptic one. This is confirmed by a spectral  
397 analysis of precipitation and meridional wind at 700 hPa over [5°-16°N, 10°W-10°E] for the  
398 CTL and PSRD simulations and [5°-28°N, 10°W-10°E] for the GSRD and GSPD  
399 simulations. The different domains, as for the wavy day calculation, reflect the northward  
400 shift of the monsoon under a Green Sahara. The northern limits are chosen to roughly match  
401 the monsoon's northernmost extent, calculated following the methodology of Pausata et al.  
402 [2016]. The CTL and PSRD meridional wind spectra display a clear peak around the AEW  
403 periodicity (2-5 days), while in the two Green Sahara scenarios the power in this band is  
404 weaker, and the spectra increase almost monotonically with period (Figure 9b). The  
405 precipitation spectra (Figure 9a) reflect this difference. In the CTL and PSRD simulations  
406 there is again a clear peak matching the AEW periodicity and highlighting the waves'  
407 dominant role in driving precipitation. In the two Green Sahara scenarios, the spectra show a  
408 roughly monotonic increase with period, suggesting that the 2-5 day band only accounts for a  
409 modest fraction of the total precipitation. . Furthermore, while longer waves in the 6-9 day  
410 band grow in importance under a green Sahara, they do not play the same role as the 2-5 day  
411 band in the desert Sahara scenarios (Figure 9). The Green Sahara simulations display a higher  
412 spectral power than the desert Sahara in both meridional wind and precipitation beyond ~6  
413 days, but there is no clear peak to suggest that a specific dynamical mechanism is acting to  
414 enhance the precipitation over this frequency range.

415

416 Summarizing, the Green Sahara scenario is characterized by a widespread increase in  
417 precipitation, accompanied by a significant reduction in the 3-5 day AEW activity and in  
418 their ability to drive precipitation. The precipitation and meridional wind spectra show a shift  
419 towards longer periods and do not display any prominent peaks. This is somewhat surprising,

420 because a sizable fraction of the present-day monsoonal precipitation is ascribed to the  
421 convection triggered by AEWs [Skinner and Diffenbaugh, 2013]. Hence, a more active AEW  
422 regime might be expected under an intensified MH monsoon, due to the increased latent heat  
423 and convection associated with the increased precipitation. This apparent contradiction can be  
424 reconciled by considering the role of the AEJ in triggering and strengthening the AEWs,  
425 through barotropic-baroclinic instabilities [Thorncroft and Hoskins, 1994]. Wu et al. [2012]  
426 found that synoptic disturbances are more likely where the zonal flow is stronger and that the  
427 more unstable waves are likely to be closer to the zonal flow maximum, i.e., closer to an  
428 intense AEJ core. It is therefore argued that, in the Green Sahara scenarios, the radical  
429 modification of the AEJ dynamics dominates the thermodynamic changes; the sizable  
430 northward migration (+6.5°) and weakening (-2.7 m/s) being more effective in shifting and  
431 suppressing the wave activity than the latent heat and convection increase in enhancing it.  
432 Finally, it is highlighted that the dust reduction induces opposite responses in the atmospheric  
433 dynamics, depending on the land cover of the Sahara: it leads to more or less favorable  
434 conditions for precipitation, when associated with a vegetated or desert surface, respectively.

435

### 436 **3.2 Energy budget**

437

438 The rainfall and atmospheric circulation patterns simulated in the sensitivity experiments are  
439 closely linked to the changes in surface conditions and radiative properties of the atmosphere,  
440 which in turn affect the energetics and dynamics of the WAM. This section elucidates the  
441 links between energetics, precipitation and dynamics in the sensitivity experiments, through  
442 the analysis of the atmospheric radiative and heat fluxes, and moist static energy (MSE)  
443 content.

444

445 The greening of the Sahara (GSPD simulation) lowers the surface albedo over a vast portion  
446 of North Africa (see Table 1), leading to an increase in the net flux of the clear-sky  
447 downward SW radiation at the top of the atmosphere (TOA) (Figure 10c). The downward  
448 SW flux anomaly is almost uniform and limited to the area where the surface albedo is  
449 lowered. The reduction in dust concentration, when the Sahara is deserted (PSRD  
450 simulation), leads to an upward SW flux anomaly at the TOA, in which the fingerprint of the  
451 dust reduction pattern is evident (Figure 10e). The upward SW flux is due to the increase in  
452 the planetary albedo produced by the removal of airborne dust over a bright surface. On the  
453 contrary, the removal of airborne dust when the Sahara is vegetated (GSRD simulation)  
454 further reduces the planetary albedo of a dark surface, enhancing the downward flux anomaly  
455 of SW radiation simulated in the GSPD experiment (Figure 10a), although the effect is quite  
456 weak (Figure 10g).

457

458 At the surface, the effect of greening the Sahara (GSPD simulation) is similar to the TOA,  
459 resulting in a positive anomaly of the downward SW radiation, limited to the area where the  
460 surface albedo is reduced (Figure 10d). A widespread increase in the downward SW radiation  
461 at the surface is also simulated in the PSRD experiment (Figure 10f), in which the removal of  
462 airborne dust reduces the absorption of the solar radiation, especially at latitudes around  
463 15°N, where dust concentration is maximum (see Figure 1). By reducing the absorption of  
464 solar radiation, the removal of airborne dust over the Green Sahara (GSRD simulation)  
465 enhances the positive anomaly in the downward SW radiation due to the lower surface albedo  
466 (Figure 10b, h).

467

468 In the Green Sahara experiments, the SW radiative forcing simulated at the surface over the  
469 Sahel and Sahara is accompanied by a negative (i.e. upward) anomaly in the sensible heat

470 (SH) flux, which reverts to positive (i.e. downward) between 10°N and 20°N due to the  
471 cooling effect of the precipitation anomalies (Figures 11a, c; cf. Figure 2). The additional SW  
472 radiative forcing in the GSRD simulation, associated with the dust reduction, limits the  
473 upward SH flux in the eastern Sahel (Figures 11a, g). In the PSRD simulation, the upward SH  
474 flux anomaly is widespread, peaking between 10°N and 20°N, where the SW radiative  
475 forcing is maximum (Figure 11e; cf. Figure 10f). The latent heat (LH) flux at the surface  
476 shows significant negative (i.e. upward) anomalies in the Green Sahara scenarios (Figures  
477 11b, d). The release of LH into the atmosphere is associated with enhanced evaporation over  
478 the vegetated surface, induced by the SW radiative forcing. The LH response is shaped by the  
479 precipitation anomalies, further enhancing evaporation (Figures 11b, d; cf. Figure 2). The  
480 reduction in dust concentration over the Green Sahara increases SW radiative forcing and  
481 precipitation at the surface, strengthening the LH release into the atmosphere (Figure 11h).

482 Reduction in dust concentration alone (PSRD simulation) results in LH release over the  
483 vegetated Sahel (south of 15°N), induced by the SW radiative forcing, while the decreased  
484 precipitation leads to negative anomalies in the LH flux north of 15°N (Figure 11f).

485

486 The combination of the LH and SH fluxes results in an intense upward heat flux over the  
487 Sahara in the Green Sahara experiments, and a weaker upward flux peaking over the Sahel in  
488 the PSRD experiment (Figure S6). The heat flux then triggers moist convection, whose  
489 modifications are diagnosed in the sensitivity experiments through the MSE content of the  
490 atmosphere. This is defined as the sum of geopotential, enthalpy and latent heat:

$$491 \quad MSE = gz + C_p T + Lq,$$

492 where  $g$  is the gravitational acceleration,  $z$  the geopotential height,  $C_p$  the specific heat of dry  
493 air at constant pressure,  $T$  temperature,  $L$  the latent heat of evaporation, and  $q$  the specific  
494 humidity. The MSE is a direct indicator of the monsoonal precipitation, because the

495 transformation of enthalpy and latent energy available in the lower troposphere into  
496 geopotential energy aloft is the main signal of convection [Fontaine and Philippon, 2000]. In  
497 the GSRD simulation, the meridional profile of the MSE atmospheric content shows an  
498 intense positive anomaly dominating the entire troposphere from 15°N to 35°N (Figure 12a).  
499 Close to the surface, at 1000 hPa, the MSE peak moves 6° northward (from 14°N in CTL to  
500 20°N; Figure S7), accompanied by an increase in the meridional difference between the peak  
501 and the Guinea Coast (+1.7 kJ/kg; Figure S7). The GSPD simulation shows a similar pattern,  
502 characterized by weaker anomalies (Figures 12 b, d): a +5° migration of the MSE peak and a  
503 1.2 kJ/kg increase in the meridional difference with the Guinea Coast (Figure S7). These  
504 modifications elucidate the precipitation response in the Green Sahara experiments: the  
505 meridional migration and intensification of the peak MSE favor the northward penetration of  
506 the precipitation belt, and the MSE excess in the lower-middle troposphere triggers deep  
507 convection over the Sahara. In the PSRD simulation (Figure 12c), the MSE content shows a  
508 negative anomaly in the middle-upper troposphere, and a weakening of the maximum close to  
509 the surface (-0.7 kJ/kg at 1000 hPa; Figure S7), resulting in a weaker monsoonal circulation.

510

#### 511 **4 Discussion and conclusions**

512

513 The objective of this study is to improve the understanding of the changes in the West  
514 African monsoon dynamics and precipitation patterns during the mid-Holocene, when large  
515 part of North Africa was characterized by a mesic environment and the Sahara desert was  
516 extensively covered by vegetation. A set of idealized sensitivity experiments, performed with  
517 the EC-Earth climate model, has been used to understand the changes in atmospheric  
518 circulation that characterized that period. In these simulations, vegetation cover over the

519 Sahara and a reduction in atmospheric mineral dust concentrations are imposed together and  
520 in turn.

521

522 By using these set of simulations, Pausata et al. [2016] showed that the vegetation cover over  
523 the Sahara is the primary driver of a radical alteration of the West African monsoon during  
524 the mid-Holocene, with the associated dust reduction further strengthening precipitation  
525 anomalies inland. The precipitation simulated in their “Green Sahara and reduced dust”  
526 experiment is indeed quantitatively consistent with estimations of the mid-Holocene  
527 precipitation based on paleoclimate proxy data [Tierney et al., 2017]. This study further  
528 extends the analysis performed by Pausata et al. [2016], to improve the understanding of the  
529 changes in the monsoonal dynamics accompanying the precipitation anomalies. The  
530 modifications of the radiative balance at the surface and the TOA are also discussed, along  
531 with the consequent response of the energetics of the monsoonal system.

532

533 When a vegetation cover is prescribed over the Sahara (GSPD), a dramatic response in the  
534 West African monsoon is simulated. The lowering of the surface albedo induces an intense  
535 positive radiative forcing at the TOA and at the surface over the Sahara, leading to a release  
536 of sensible and latent heat into the atmosphere. The heat flux anomaly triggers moist  
537 convection over this region, driving a northward expansion of the monsoonal precipitation  
538 belt, which extends up to the Mediterranean coast. A substantial modification of the regional  
539 circulation is also simulated, with critical alterations in some of the “classical” dynamical  
540 features of the West African monsoon, such as the Saharan heat low, the African easterly jet,  
541 and the African easterly wave regime. In particular, a weakening of the African easterly wave  
542 activity is associated with a decrease in wave-related precipitation, suggesting a reduction of  
543 the African easterly waves’ role in triggering and organizing mesoscale convective systems.

544 These changes follow a general reorganization of the circulation towards a cyclonic gyre  
545 throughout the troposphere. This analysis suggests that a vegetated Sahara may radically  
546 change the regional circulation pattern over West Africa.

547

548 On the opposite, dust reduction alone (PSRD) leads to a slight weakening in the monsoonal  
549 circulation and precipitation rates. This weakening is associated with a positive surface  
550 radiative forcing in the Sahel and a radiative cooling in the middle-upper troposphere over the  
551 Sahara, resulting in a reduction of the meridional energy gradient over West Africa, which  
552 prevent monsoonal precipitation to penetrate inland.

553

554 The effect of dust removal on the radiative balance of the atmosphere depends on the  
555 radiative properties of the airborne dust in association with the underlying land cover. Indeed,  
556 in PI conditions dust reduction increases the planetary albedo above the Sahara desert,  
557 cooling the middle-upper troposphere, and induces a positive radiative forcing at the surface,  
558 peaking in the vegetated Sahel. On the contrary, when a vegetated surface is prescribed from  
559 the Sahel to the Sahara, dust reduction lowers the planetary albedo, warming the middle-  
560 upper troposphere, and induces a positive radiative forcing at the surface, peaking in the  
561 Sahel-Sahara transition zone where PI dust concentration is maximum.

562

563 The radical modification of the atmospheric circulation over North Africa discussed in this  
564 study is likely to have triggered a chain of global-scale changes during the mid-Holocene. For  
565 example, Muschitiello et al. [2015], using the same model as in this study, show that the  
566 desertification of the Sahara at the end of the African humid period led to a reduction in the  
567 atmospheric and oceanic poleward heat transport from tropical to high northern latitudes. The  
568 reduction in the poleward heat transport weakened the mid-latitude westerlies, resulting in

569 more negative Arctic Oscillation-like conditions and a consequent cooling over the Arctic  
570 and North Atlantic regions. Results presented in this paper show that the greening of the  
571 Sahara triggers a strong reduction in African easterly wave activity, which is known to be  
572 related with the formation of tropical cyclones in the Atlantic Ocean [Price et al., 2015].  
573 Therefore, the decreased AEW activity may induce a reduction in tropical storms developing  
574 in the North Atlantic. On the other hand, the reduction in the Saharan dust emission and  
575 transport across the tropical Atlantic is favorable to the development of tropical cyclones in  
576 the basin, through the radiative warming of the ocean surface [Evan et al., 2006], indicating  
577 possible competing effects of the vegetation-dust changes in the Sahara on the Atlantic  
578 hurricane season. Furthermore, reducing African easterly waves may initially lead to fewer  
579 tropical cyclones but, because of that, the ocean would warm, compensating for the reduced  
580 wave activity (assuming no other changes in the thermodynamic structure of the atmosphere).  
581 Therefore, the combination of Sahara greening and reduced dust emission during the mid-  
582 Holocene may have led to an increased number of tropical cyclones in the Atlantic. By  
583 analyzing the same set of simulations used in this study, Pausata et al. [2017a] show indeed  
584 an increase in the tropical cyclone activity in both the hemispheres and particularly over the  
585 Caribbean basin and the east coast of North America. This hypothesis cannot be tested with  
586 current paleotempestology archives that are geographically and temporally patchy, and hence  
587 unable to provide a complete view of the Holocene storm activity. However, a proxy-data  
588 reconstruction from Puerto Rico suggests a positive correlation between West African  
589 monsoon strength and tropical cyclone intensity over the last 5500 years [Donnelly &  
590 Woodruff, 2008]. In particular, the period between 2500 and 1000 years BP was the most  
591 active tropical storm interval in Puerto Rico and was characterized by a stronger WAM and a  
592 reduced Saharan dust flux relative to the following millennium [Mulitza et al., 2010]. In  
593 addition, Williams et al. [2016] emphasized the relationship between reduced dust loading

594 during the early and mid-Holocene and the northward expansion of the ITCZ, which in turn  
595 can intensify tropical storm activity in the western North Atlantic [van Hengstum et al.,  
596 2016]. Pausata et al. [2017b] also show reduced El Niño-Southern Oscillation (ENSO)  
597 variability and La Niña-like conditions in winter in a Green Sahara scenario, compared to  
598 pre-industrial and the standard CMIP/PMIP mid-Holocene scenarios. These changes in  
599 ENSO mean state and variability are in general favorable to tropical storm activity in the  
600 North Atlantic basin [Chiacchio et al., 2017]. Further efforts both from the modelling and the  
601 proxy community are necessary to better understand the remote teleconnections associated to  
602 the West African monsoon variability.

603

604 The findings of this study are also useful also in a future perspective, at regional and global  
605 scales. Indeed, the possible positive trend in Sahelian precipitation projected for the 21st  
606 century [Biasutti, 2013] may be accompanied and amplified by land cover and dust reduction  
607 feedbacks, which in turn may impact climate in remote regions.

608

## 609 **Acknowledgements**

610

611 M. G. has been supported by the LABEX project, funded by Agence Nationale de la  
612 Recherche (French National Research Agency, grant ANR-10-LABX-18-01). G. M. has been  
613 supported by the MILEX project, funded by the Swedish Research Council (Vetenskapsrådet  
614 grant 2012-40395-98427-17) and a grant from the Department of Meteorology of Stockholm  
615 University. Q.Z. acknowledges funding from Swedish Research Council VR for the Swedish-  
616 French project “Greenland in a warming Arctic”. F.S.R.P. acknowledges funding from the  
617 Swedish Research Council (FORMAS) as part of the Joint Programming Initiative on  
618 Climate and the Belmont Forum for the project “Palaeo-constraints on Monsoon Evolution

619 and Dynamics (PACMEDY)” (grant FR-2016/0001). The simulations with EC-Earth were  
620 performed on supercomputer provided by the Swedish National Infrastructure for Computing  
621 (SNIC) at NSC and Cray XC30 HPC systems at ECMWF. The authors thank three  
622 anonymous reviewers for their constructive comments, which led to a substantial  
623 improvement of the manuscript.

624

625 **References**

626

627 Albani, S., N. M. Mahowald, A. T. Perry, R. A. Scanza, C. S. Zender, N. G. Heavens, V.

628 Maggi, J. F. Kok, and B. L. Otto-Bliesner (2014), Improved dust representation in the

629 Community Atmosphere Model, *J. Adv. Model. Earth Syst.*, 6, 541–570,

630 doi:10.1002/2013MS000279.

631 Biasutti, M. (2013), Forced Sahel rainfall trends in the CMIP5 archive, *J. Geophys. Res.*

632 *Atmos.*, 118, 1613–1623, doi:10.1002/jgrd.50206.

633 Biasutti, M., A. H. Sobel, and S. J. Camargo (2009), The Role of the Sahara Low in

634 Summertime Sahel Rainfall Variability and Change in the CMIP3 Models, *J. Clim.*, 22,

635 5755–5771, doi:10.1175/2009JCLI2969.1.

636 Braconnot, P., S.P. Harrison, B. Otto-Bliesner, A. Abe-Ouchi, J. Jungclaus, and J.Y.

637 Peterschmitt (2011), The Paleoclimate Modeling Intercomparison Project contribution to

638 CMIP5, CLIVAR Exchanges No. 56, 16, 15-19.

639 Chen, T. C. (2005), Maintenance of the midtropospheric North African summer circulation;

640 Saharan high and African easterly jet, *J. Clim.*, 18, 2943–2962, doi:10.1175/JCLI3446.1.

641 Chiacchio, M., F. S. R. Pausata, G. Messori, A. Hannachi, M. Chin, T. Önskog, A. M. L.

642 Ekman, and L. Barrie (2017), On the links between meteorological variables, aerosols,

643 and tropical cyclone frequency in individual ocean basins, *J. Geophys. Res. Atmos.*,

644 122, 802–822, doi:10.1002/2015JD024593.

645 Claussen, M. and V. Gayler (1997), The greening of the Sahara during the mid-Holocene:

646 results of an interactive atmosphere-biome model, *Global Ecology and Biogeography*

647 *Letters*, 6, 369-377.

648 deMenocal, P. B., J. Ortiz, T. Guilderson, J. Adkins, M. Sarnthein, L. Baker, and M.

649 Yarusinsky (2000), Abrupt onset and termination of the African Humid Period: Rapid

650 climate responses to gradual insolation forcing, *Quat. Sci. Rev.*, 19, 347–361,  
651 doi:10.1016/S0277-3791(99)00081-5.

652 Diedhiou A., S. Janicot, A. Viltard, P. de Felice, and H. Laurent (1998), Evidence of two  
653 regimes of easterly waves over West Africa and the tropical Atlantic. *Geophys. Res.*  
654 *Let.*, 25, 2805-2808.

655 Diedhiou A., S. Janicot, A. Viltard, P. De Felice, and H. Laurent (1999), Easterly waves  
656 regimes and associated convection over West Africa and the tropical Atlantic: results  
657 from the NCEP/NCAR and ECMWF reanalyses. *Clim. Dyn.*, 15, 795-822.

658 Donnelly, J. P. and J. D. Woodruff (2007), Intense hurricane activity over the past 5,000  
659 years controlled by El Niño and the West African monsoon, *Nature*, 447, 465-468.

660 ECMWF (2010), ECMWF Newsletter No. 126, Winter 2010/11  
661 ([http://www.ecmwf.int/sites/default/files/elibrary/2010/14597-newsletter-no126-winter-](http://www.ecmwf.int/sites/default/files/elibrary/2010/14597-newsletter-no126-winter-201011.pdf)  
662 [201011.pdf](http://www.ecmwf.int/sites/default/files/elibrary/2010/14597-newsletter-no126-winter-201011.pdf)).

663 Egerer, S., M. Claussen, C. Reick, and T. Stanelle (2016), The link between marine sediment  
664 records and changes in Holocene Saharan landscape: simulating the dust cycle, *Clim.*  
665 *Past*, 12, 1009-1027, doi:10.5194/cp-12-1009-2016.

666 Evan, A. T., J. Dunion, J. A. Foley, A. K. Heidinger, and C. S. Velden (2006), New evidence  
667 for a relationship between Atlantic tropical cyclone activity and African dust outbreaks,  
668 *Geophys. Res. Lett.*, 33, L19813, doi:10.1029/2006GL026408.

669 Evan A.T., C. Flamant, M. Gaetani, and F. Guichard (2016), The Past, Present and Future of  
670 African Dust. *Nature*, 531, 493-495, doi:10.1038/nature17149.

671 Fontaine, B., and N. Philippon (2000), Seasonal Evolution of Boundary Layer Heat Content  
672 in the West African Monsoon From the NCEP/NCAR, *Int. J. Climatol.*, 20, 1777–1790.

673 Gaetani, M., C. Flamant, S. Bastin, S. Janicot, C. Lavaysse, F. Hourdin, P. Braconnot, S.  
674 Bony (2016), West African monsoon dynamics and precipitation: the competition

675 between global SST warming and CO2 increase in CMIP5 idealized simulations, *Clim.*  
676 *Dyn.*, doi:10.1007/s00382-016-3146-z.

677 Gasse, F. (2000), Hydrological changes in the African tropics since the Last Glacial  
678 Maximum. *Quat. Sci. Rev.*, 19, 189–211.

679 Giannini, A. (2010), Mechanisms of Climate Change in the Semiarid African Sahel: The  
680 Local View, *J. Clim.*, 23, 743–756, doi:10.1175/2009JCLI3123.1.

681 Ginoux, P., J. M. Prospero, T. E. Gill, N. C. Hsu, and M. Zhao (2012), Global-scale  
682 attribution of anthropogenic and natural dust sources and their emission rates based on  
683 MODIS Deep Blue aerosol products, *Rev. Geophys.*, 50, 1–36,  
684 doi:10.1029/2012RG000388.

685 Gu, G., R. F. Adler, G. J. Huffman, and S. Curtis (2004), African easterly waves and their  
686 association with precipitation, *J. Geophys. Res.*, 109, D04101,  
687 doi:10.1029/2003JD003967.

688 Harrison, S. P., P. J. Bartlein, S. Brewer, I. C. Prentice, M. Boyd, I. Hessler, K. Holmgren, K.  
689 Izumi, and K. Willis (2014), Climate model benchmarking with glacial and mid-  
690 Holocene climates, *Clim. Dyn.*, 43, 671–688, doi:10.1007/s00382-013-1922-6.

691 Harrison, S.P., P.J. Bartlein, K. Izumi, G. Li, J. Annan, J. Hargreaves, P. Braconnot, M.  
692 Kageyama (2015), Evaluation of CMIP5 palaeo-simulations to improve climate  
693 projections, *Nat. Clim. Change*, 5, 735–743, doi:http://dx.doi.org/10.1038/  
694 nclimate2649.

695 Hazeleger, W., et al. (2010), EC-Earth: A Seamless Earth-System Prediction Approach in  
696 Action, *Bull. Am. Meteorol. Soc.*, 91, 1357–1363, doi:10.1175/2010BAMS2877.1.

697 Hély, C., A.-M. Lézine, and APD contributors (2014), Holocene changes in African  
698 vegetation: tradeoff between climate and water availability, *Clim. Past*, 10, 681–686,  
699 doi:10.5194/cp-10-681-2014.

700 Holmes, J. A., (2008), How the Sahara became dry. *Science* 320, 752–753,  
701 doi:10.1126/science.1158105.

702 IFAD (2013), Rainfed Food Crops in West and Central Africa : Rainfed Food Crops in West  
703 and Central Africa, A Savoir, July 2013.

704 Kröpelin, S., D. Verschuren, A.-M. Lézine, H. Eggermont, C. Cocquyt, P. Francus, J.-P.  
705 Cazet, M. Fagot, B. Rumes, J.M. Russell, F.Darius, D.J. Conley, M. Schuster, H. von  
706 Suchodoletz, D.R. Engstrom (2008), Climate-driven ecosystem succession in the  
707 Sahara: the past 6000 years, *Science*, 320, 765-768,  
708 <http://dx.doi.org/10.1126/science.1154913>.

709 Lavaysse, C., C. Flamant, S. Janicot, D. J. Parker, J. P. Lafore, B. Sultan, and J. Pelon (2009),  
710 Seasonal evolution of the West African heat low : a climatological perspective, *Clim.*  
711 *Dyn.*, 33, 313–330.

712 Levis, S., Bonan G. B., and Bonfils C. (2004), Soil feedback drives the mid-Holocene North  
713 African monsoon northward in fully coupled CCSM2 simulations with a dynamic  
714 vegetation model, *Clim. Dyn.*, 23, 791-802, doi:10.1007/s00382-004-0477-y.

715 Lézine, A.-M., C. Hély, C. Grenier, P. Braconnot, and G. Krinner (2011), Sahara and Sahel  
716 vulnerability to climate changes, lessons from Holocene hydrological data, *Quat. Sci.*  
717 *Rev.*, 30, 3001–3012, doi:10.1016/j.quascirev.2011.07.006.

718 Madec, G. (2008), NEMO ocean engine, Note du Pole de modlisation, Institut Pierre-Simon  
719 Laplace (IPSL), Paris, France, No. 27, ISSN No. 1288-1618  
720 (<http://www.nemoocean.eu/About-NEMO/Reference-manuals>).

721 McGee, D., P. B. deMenocal, G. Winckler, J. B. W. Stuut, and L. I. Bradtmiller (2013), The  
722 magnitude, timing and abruptness of changes in North African dust deposition over the  
723 last 20,000yr, *Earth Planet. Sci. Lett.*, 371-372, 163–176,  
724 doi:10.1016/j.epsl.2013.03.054.

725 Mulitza, S., D. Heslop, D. Pittauerova, H.W. Fischer, I. Meyer, J.-B. Stuut, M. Zabel, G.  
726 Mollenhauer, J.A. Collins, H. Kuhnert and M. Schulz (2010), Increase in African dust  
727 flux at the onset of commercial agriculture in the Sahel region, *Nature*, 466, 226-228.

728 Muschitiello, F., Q. Zhang, H. S. Sundqvist, F. J. Davies, and H. Renssen (2015), Arctic  
729 climate response to the termination of the African Humid Period, *Quaternary Science*  
730 *Reviews*, 125, 91-97, doi:10.1016/j.quascirev.2015.08.012.

731 Nicholson, S. E. (2013), The West African Sahel: A Review of Recent Studies on the  
732 Rainfall Regime and Its Interannual Variability, *ISRN Meteorol.*, 2013, 453521,  
733 doi:10.1155/2013/453521.

734 Patricola, C. M., and K. H. Cook (2007), Dynamics of the West African Monsoon under Mid-  
735 Holocene Precessional Forcing: Regional Climate Model Simulations, *J. Clim.*, 20, 694-  
736 716, doi:10.1175/JCLI4013.1.

737 Patricola, C. M., and K. H. Cook (2008), Atmosphere/vegetation feedbacks: A mechanism  
738 for abrupt climate change over northern Africa, *J. Geophys. Res.*, 113, D18102,  
739 doi:10.1029/2007JD009608.

740 Pausata, F. S. R., K. A. Emanuel, M. Chiacchio, G. T. Diro, Q. Zhang, L. Sushama, J. C.  
741 Stager, and J. P. Donnelly (2017a), Tropical cyclone activity enhanced by Sahara  
742 greening and reduced dust emissions during the African Humid Period. *Proc. Natl.*  
743 *Acad. Sci.*, doi:10.1073/pnas.1619111114.

744 Pausata, F. S. R., G. Messori, and Q. Zhang (2016), Impacts of dust reduction on the  
745 northward expansion of the African monsoon during the Green Sahara period, *Earth*  
746 *Planet. Sci. Lett.*, 434, 298–307, doi:10.1016/j.epsl.2015.11.049.

747 Pausata F. S. R., Q. Zhang, F. Muschitiello, Z. Lu, L. Chafik, E.M. Niedermeyer, J.C. Stager,  
748 K.M. Cobb, and Z. Liu (2017b), Greening of the Sahara suppressed ENSO activity  
749 during the Mid-Holocene, *Nature Communications*, in press.

750 Price, C., N. Reicher, and Y. Yair (2015), Do West African thunderstorms predict the  
751 intensity of Atlantic hurricanes?, *Geophys. Res. Lett.*, 42, 2457–2463,  
752 doi:10.1002/2014GL062932.

753 Rachmayani, R., M. Prange, and M. Schulz (2015), North African vegetation-precipitation  
754 feedback in early and mid-Holocene climate simulations with CCSM3-DGVM, *Clim.*  
755 *Past.*, 11, 175–185, doi:10.5194/cp-11-175-2015.

756 Rodríguez-Fonseca, B., et al. (2015), Variability and Predictability of West African  
757 Droughts: A Review on the Role of Sea Surface Temperature Anomalies, *J. Clim.*, 28,  
758 4034–4060, doi:10.1175/JCLI-D-14-00130.1.

759 Roehrig, R., D. Bouniol, F. Guichard, F. D. Hourdin, and J. L. Redelsperger (2013), The  
760 present and future of the west african monsoon: A process-oriented assessment of  
761 CMIP5 simulations along the AMMA transect, *J. Clim.*, 26, 6471–6505,  
762 doi:10.1175/JCLI-D-12-00505.1.

763 Rowell, D. P. (2013), Simulating SST teleconnections to Africa: What is the state of the art?,  
764 *J. Clim.*, 26, 5397–5418, doi:10.1175/JCLI-D-12-00761.1.

765 Schmidt, G. A., et al. (2014), Using palaeo-climate comparisons to constrain future  
766 projections in CMIP5, *Clim. Past.*, 10, 221–250, doi:10.5194/cp-10-221-2014.

767 Shanahan, T.M., J.T. Overpeck, C.W. Wheeler, J.W. Beck, J.S. Pigati, M.R. Talbot, C. A.  
768 Scholz, J. Peckh, J. W. Kingi (2006), Paleoclimatic variations in West Africa from a  
769 record of late Pleistocene and Holocene lake level stands of Lake Bosumtwi, Ghana.  
770 *Palaeogeography, Palaeoclimatology, Palaeoecology*, 242, 287-302,  
771 doi:10.1016/j.palaeo.2006.06.007

772 Skinner, C. B., and N. S. Diffenbaugh (2013), The contribution of African easterly waves to  
773 monsoon precipitation in the CMIP3 ensemble, *J. Geophys. Res. Atmos.*, 118, 3590–  
774 3609, doi:10.1002/jgrd.50363.

775 Skinner, C. B., and C. J. Poulsen (2016), The role of fall season tropical plumes in enhancing  
776 Saharan rainfall during the African Humid Period, *Geophys. Res. Lett.*, 43, 349–358,  
777 doi:10.1002/2015GL066318.

778 Su, H., and J. D. Neelin (2005), Dynamical mechanisms for African monsoon changes during  
779 the mid-Holocene, *J. Geophys. Res.*, 110, D19105, doi:10.1029/2005JD005806

780 Sultan, B., and M. Gaetani (2016), Agriculture in West Africa in the Twenty-First Century:  
781 Climate Change and Impacts Scenarios, and Potential for Adaptation. *Front. Plant Sci.*,  
782 7, 1262, doi:10.3389/fpls.2016.01262.

783 Swann, A. L. S., I. Y. Fung, Y. Liu, and J. C. H. Chiang (2014), Remote Vegetation  
784 Feedbacks and the Mid-Holocene Green Sahara, *J. Clim.*, 27, 4857-4870,  
785 doi:10.1175/JCLI-D-13-00690.1.

786 Taylor, K. E., R. J. Stouffer, and G. A. Meehl (2012), An overview of CMIP5 and the  
787 experiment design, *Bull. Am. Meteorol. Soc.*, 93, 485–498, doi:10.1175/BAMS-D-11-  
788 00094.1.

789 Thorncroft, C. D., and M. Blackburn (1999), Maintenance of the African easterly jet, *Q. J. R.*  
790 *Meteorol. Soc.*, 125, 763-786, doi:10.1002/qj.49712555502.

791 Thorncroft, C. D., and B. J. Hoskins (1994), An idealized study of African easterly waves. I:  
792 A linear view. *Q.J.R. Meteorol. Soc.*, 120: 953–982. doi:10.1002/qj.49712051809.

793 Tierney, J. E., F. S. R. Pausata, and P. B. deMenocal (2017), Rainfall regimes of the Green  
794 Sahara. *Sci. Adv.*, 3: e1601503, doi:10.1126/sciadv.1601503

795 Valcke, S. (2006), OASIS3 user guide, PRISM Tech. Rep. 3, 64 pp., Partnership for Res.  
796 Infrastructures in Earth System Modeling, Toulouse, France  
797 ([http://www.prism.enes.org/Publications/Reports/oasis3\\_UserGuide\\_T3.pdf](http://www.prism.enes.org/Publications/Reports/oasis3_UserGuide_T3.pdf)).

798 Vancoppenolle, M., T. Fichefet, H. Goosse, S. Bouillon, G. Madec, and M. A. Morales  
799 Maqueda (2008), Simulating the mass balance and salinity of Arctic and Antarctic sea

800 ice. 1. Model description and validation, *Ocean Model.*, 27, 33-53,  
801 doi:10.1016/j.ocemod.2008.10.005.

802 van den Hurk, B., P. Viterbo, A. Beljaars, and A.K. Betts (2000), Offline validation of the  
803 ERA-40 surface scheme, ECMWF Tech. Memo. No. 295, ECMWF, Reading, UK.

804 van Hengstum P. J., J. P. Donnelly, P. L. Fall, M. R. Toomey, N. A. Albury, and B. Kakuk  
805 (2016), The intertropical convergence zone modulates intense hurricane strikes on the  
806 western North Atlantic margin, *Sci. Rep.*, 6, 21728.

807 Williams R.H., D. McGee, C. W. Kinsley, D. A. Ridley, S. Hu, A. Fedorov, I. Tal, R. W.  
808 Murray, and P. B. deMenocal (2016), Glacial to Holocene changes in trans-Atlantic  
809 Saharan dust transport and dust-climate feedbacks, *Sci. Adv.*, 2, e1600445,  
810 doi:10.1126/sciadv.1600445

811 Wu, M.-L.C., O. Reale, S.D. Schubert, M.J. Suarez, R.D. Koster, and Philip J. Pegion (2009),  
812 African Easterly Jet: Structure and Maintenance, *J. Climate*, 22, 4459-4480,  
813 doi:10.1175/2009JCLI2584.1.

814 Wu, M.-L.C., O. Reale, S.D. Schubert, M.J. Suarez, and Chris D. Thorncroft (2012), African  
815 Easterly Jet: Barotropic Instability, Waves, and Cyclogenesis, *J. Climate*, 25, 1489-  
816 1510, doi:10.1175/2011JCLI4241.1.

817

818 **Tables**

819

820 Table 1: Experimental design used in the control simulation (CTL) and the sensitivity  
 821 experiments: present-day Sahara and reduced dust (PSRD); Green Sahara and reduced dust  
 822 (GSRD); Green Sahara and pre-industrial dust (GSPD).

Simulation	Orbital forcing (years BP)	GHGs	Vegetation type	Albedo	LAI	Saharan dust
CTL	6k	MH	Desert	0.30	0	PI
PSRD	6k	MH	Desert	0.30	0	80% reduced
GSRD	6k	MH	Evergreen shrub	0.15	2.6	80% reduced
GSPD	6k	MH	Evergreen shrub	0.15	2.6	PI

823

824 **Figures**

825

826 Figure 1: (left) JJAS pre-industrial dust mixing ratio [kg/kg], prescribed in the CTL and  
827 GSPD simulations, and (right) difference between reduced dust and pre-industrial  
828 concentration. (a, b) Column integral, (c, d) vertical profile averaged in the range [15°W,  
829 25°E], (e, f) meridional profile of the column integral.

830

831 Figure 2: JJAS precipitation [mm/day]: (left) climatological means for the CTL simulation  
832 and the sensitivity experiments, and (right) differences between the sensitivity experiments  
833 and the CTL simulation. In panel (h), the difference between the GSRD and GSPD  
834 experiments is shown. Significance at 95% confidence level is displayed.

835

836 Figure 3: JJAS wind field at 925 hPa [m/s]: (left) climatological means for the CTL  
837 simulation and the sensitivity experiments, and (right) differences between the sensitivity  
838 experiments and the CTL simulation. In panel (h), the difference between the GSRD and  
839 GSPD experiments is shown. Significance at 95% confidence level is displayed. Shadings  
840 indicate the Saharan heat low location and intensity, represented through the values of air  
841 temperature at 850 hPa [K] exceeding the 90th percentile in the domain [0-40°N, 20°W-  
842 20°E] [Lavaysse et al., 2009]. The SHL position and intensity is determined by detecting the  
843 maximum of the air temperature at 850 hPa inside the domain.

844

845 Figure 4: JJAS wind field at 700 hPa [m/s]: (left) climatological means for the CTL  
846 simulation and the sensitivity experiments, and (right) differences between the sensitivity  
847 experiments and the CTL simulation. In panel (h), the difference between the GSRD and  
848 GSPD experiments is shown. Significance at 95% confidence level is displayed. Shadings

849 indicate the Saharan high location and intensity, represented through the geopotential height  
850 at 700 hPa exceeding 3150 m. Red lines represent the mean positions of the African easterly  
851 jet in the CTL simulation (dashed) and the sensitivity experiments (solid). The mean axis of  
852 the African easterly jet is determined in the domain [20°W-20°E, 0°-40°N] by detecting, at  
853 each longitude, the latitudinal location of the minimum of the zonal wind at 700 hPa, and  
854 averaging along the zonal direction.

855

856 Figure 5: JJAS wind field at 200 hPa [m/s]: (left) climatological means for the CTL  
857 simulation and the sensitivity experiments, and (right) differences between the sensitivity  
858 experiments and the CTL simulation. In panel (h), the difference between the GSRD and  
859 GSPD experiments is shown. Significance at 95% confidence level is displayed.

860

861 Figure 6: JJAS meridional overturning circulation, represented through the meridional wind  
862 [m/s] and the vertical velocity [Pa/s], averaged in the range [10°W, 10°E]: (left)  
863 climatological means for the CTL simulation and the sensitivity experiments, and (right)  
864 differences between the sensitivity experiments and the CTL simulation. In panel (h), the  
865 difference between the GSRD and GSPD experiments is shown. Significance at 95%  
866 confidence level is displayed.

867

868 Figure 7: JJAS African easterly wave activity, represented through the variance of the  
869 meridional wind at 700 hPa filtered in the 2.5-5-day band [m<sup>2</sup>/s<sup>2</sup>]: (left) climatological means  
870 for the CTL simulation and the sensitivity experiments, and (right) differences between the  
871 sensitivity experiments and the CTL simulation. In panel (h), the difference between the  
872 GSRD and GSPD experiments is shown. Significance at 95% confidence level is displayed,  
873 computed by using a two-sample F test.

874

875 Figure 8: Precipitation associated with the African easterly waves detected in JJAS at  
876 locations indicated by black crosses: (left) precipitation anomalies [mm/day] compared to the  
877 JJAS climatology, and (right) fraction of the JJAS total precipitation. In brackets at the top of  
878 each panel, values and fraction of the peak precipitation anomaly to the west of the black  
879 crosses. Only values in a 15° latitudinal band around the maximum of the meridional wind  
880 variance (see Figure 7) are displayed.

881

882 Figure 9: Fast Fourier transform analysis of grid-point JJAS daily (a) precipitation and (b)  
883 meridional wind at 700 hPa, averaged over [5°-16°N, 10°W-10°E] for the CTL and PSRD  
884 simulations and [5°-28°N, 10°W-10°E] for the GSRD and GSPD simulations.

885

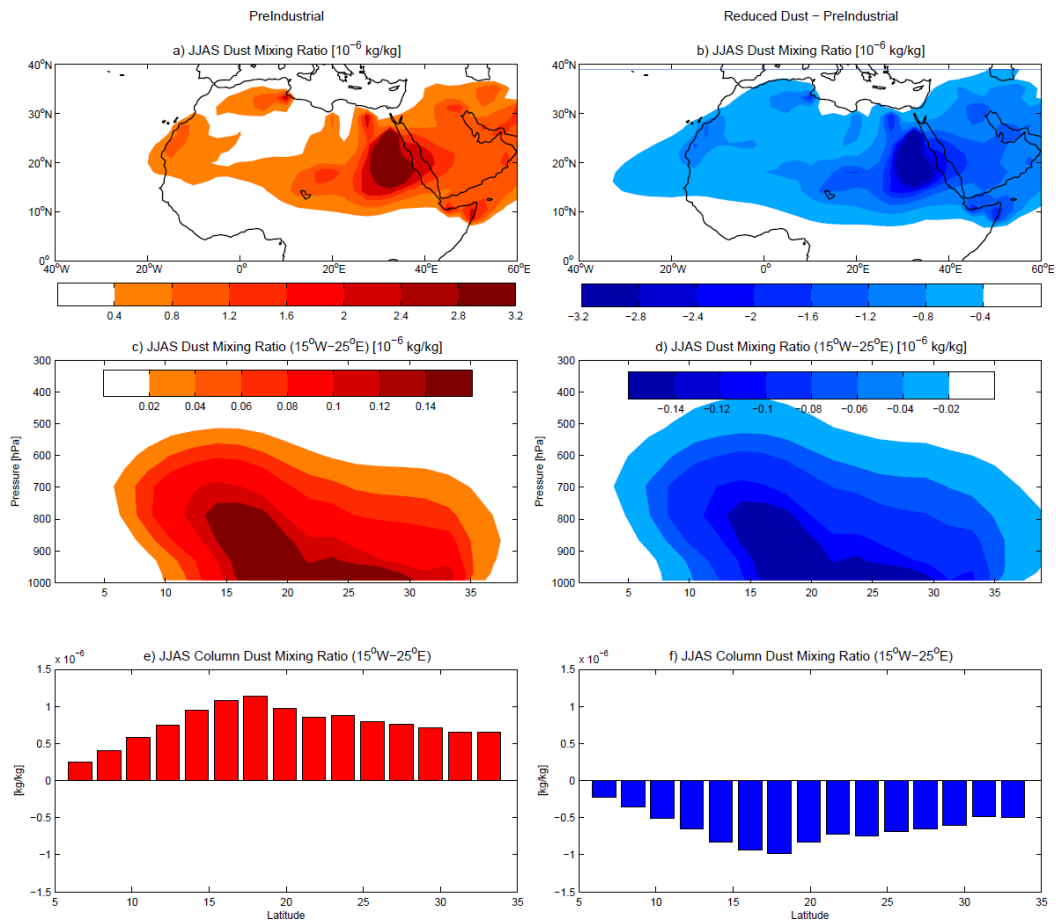
886 Figure 10: JJAS clear-sky SW radiation net flux [ $\text{W}/\text{m}^2$ ] at (left) TOA and (right) surface:  
887 (1st-3rd row) differences between the sensitivity experiments and the CTL simulation, (4th  
888 row) GSRD-GSPD difference. Significance at 95% confidence level is displayed. Radiation  
889 is represented as 24-h means, positive values indicate downward net flux. The black rectangle  
890 represents the domain where the change in land cover is applied in the Green Sahara  
891 experiments. Blue contours display the dust column concentration anomaly in the reduced  
892 dust experiments (contours at -2, -1.5, -1, -0.5 mg/kg; see Figure 1b).

893

894 Figure 11: JJAS surface (left) sensible and (right) latent heat flux [ $\text{W}/\text{m}^2$ ]: (1st-3rd row)  
895 differences between the sensitivity experiments and the CTL simulation, (4th row) GSRD-  
896 GSPD difference. Significance at 95% confidence level is displayed. Positive values indicate  
897 downward flux.

898

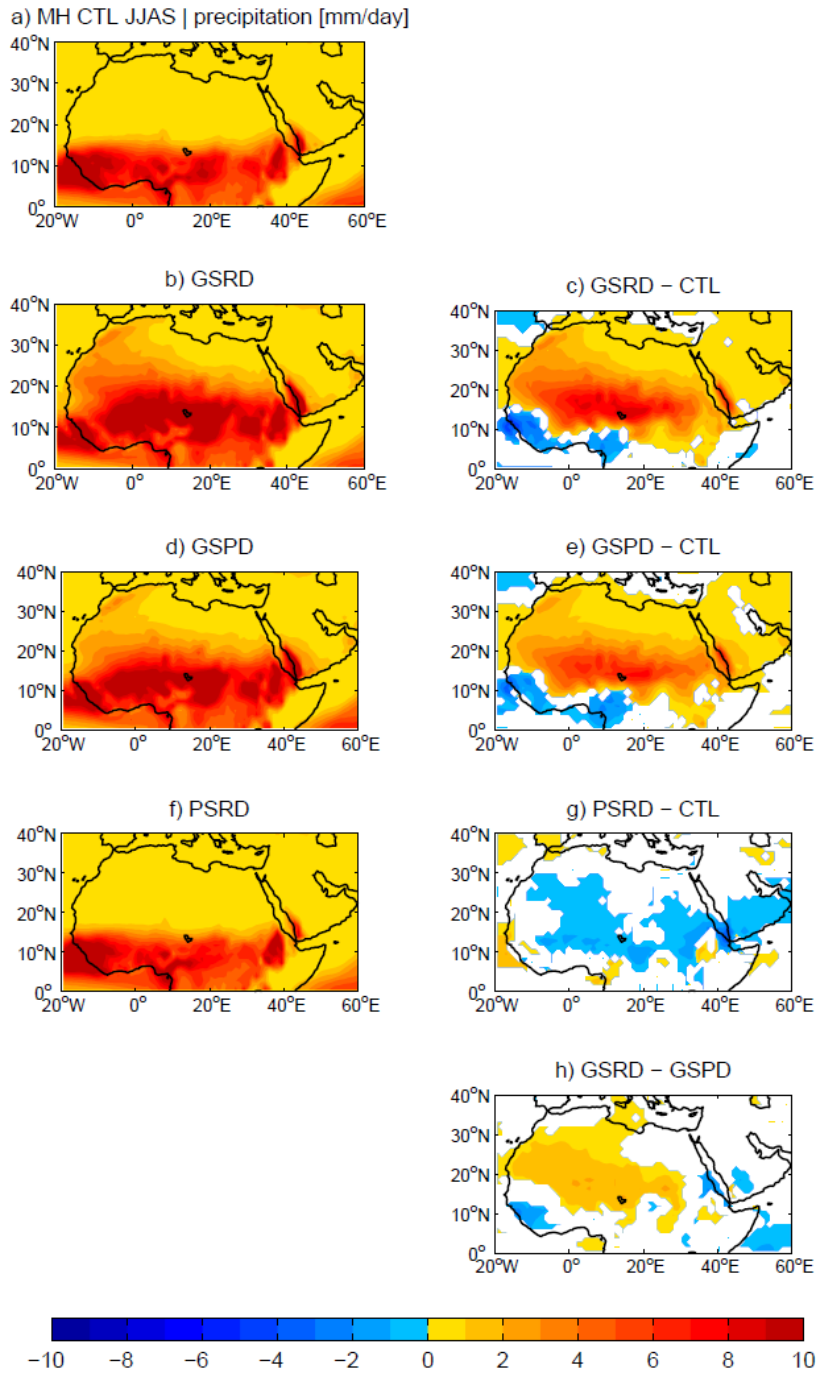
899 Figure 12: JJAS moist static energy [kJ/kg], averaged between 15°W and 25°E: (a-c)  
900 differences between the sensitivity experiments and the CTL simulation are displayed in  
901 panels, and (c) GSRD-GSPD difference. Significance at 95% confidence level is displayed.  
902



903

904 Figure 1: (left) JJAS pre-industrial dust mixing ratio [kg/kg], prescribed in the CTL and  
 905 GSPD simulations, and (right) difference between reduced dust and pre-industrial  
 906 concentration. (a, b) Column integral, (c, d) vertical profile averaged in the range [15°W,  
 907 25°E], (e, f) meridional profile of the column integral.

908



909

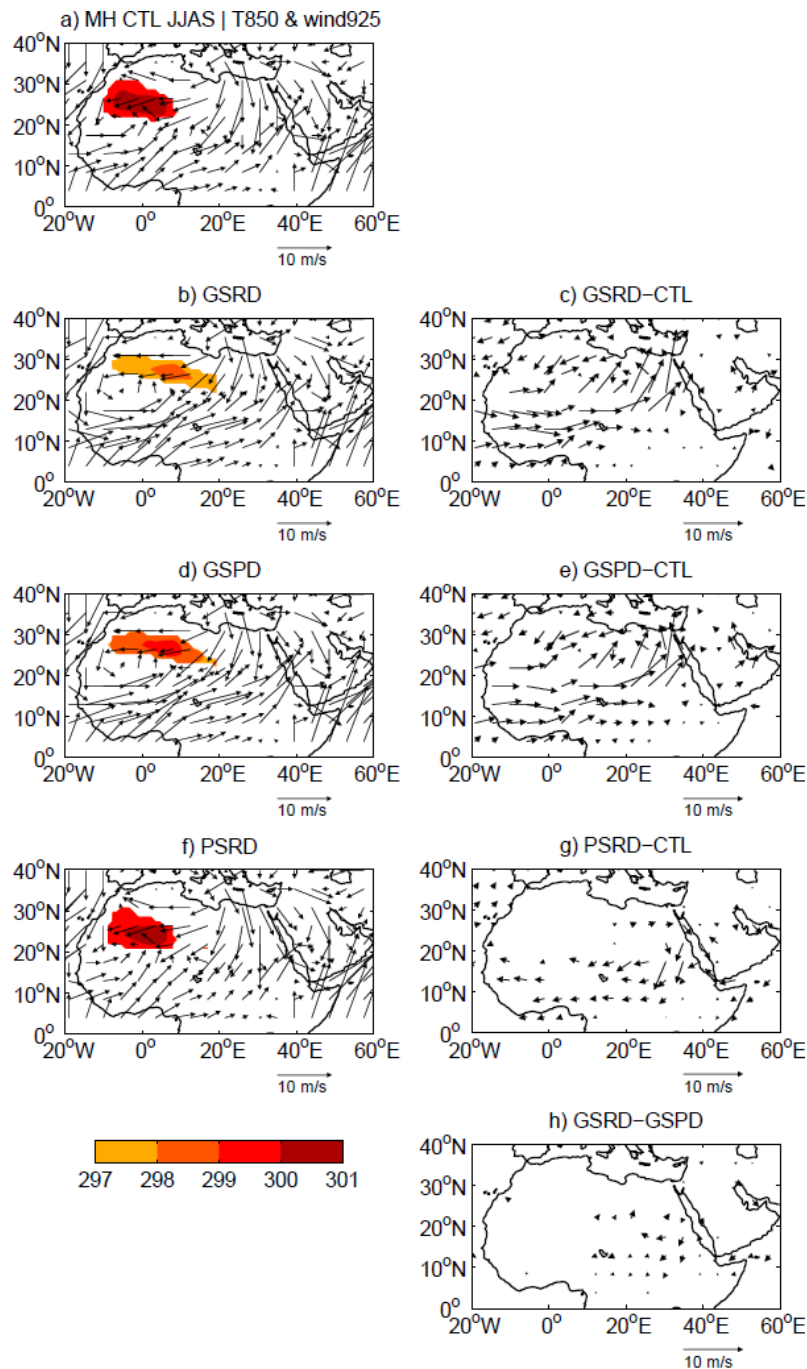
910 Figure 2: JJAS precipitation [mm/day]: (left) climatological means for the CTL simulation

911 and the sensitivity experiments, and (right) differences between the sensitivity experiments

912 and the CTL simulation. In panel (h), the difference between the GSRD and GSPD

913 experiments is shown. Significance at 95% confidence level is displayed.

914

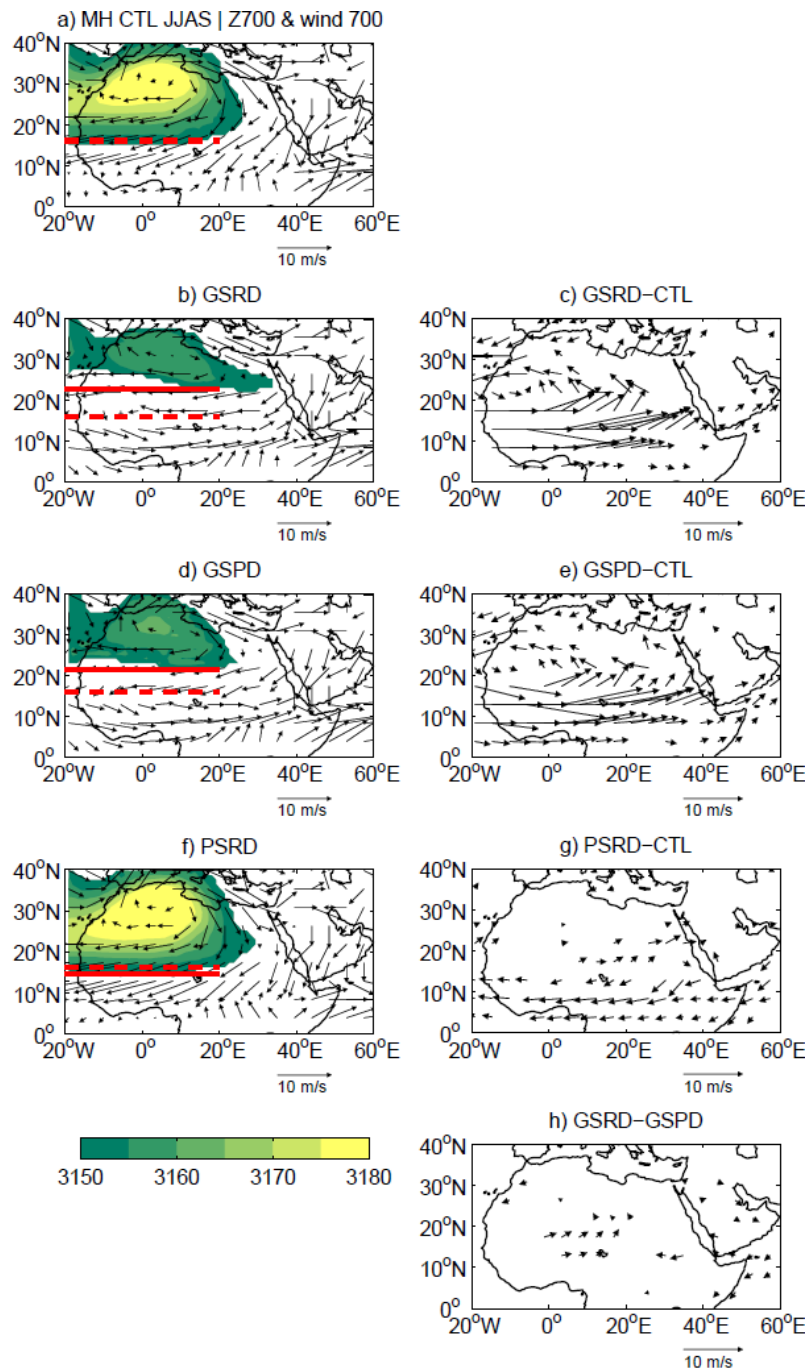


915

916 Figure 3: JJAS wind field at 925 hPa [m/s]: (left) climatological means for the CTL  
 917 simulation and the sensitivity experiments, and (right) differences between the sensitivity  
 918 experiments and the CTL simulation. In panel (h), the difference between the GSRD and  
 919 GSPD experiments is shown. Significance at 95% confidence level is displayed. Shadings  
 920 indicate the Saharan heat low location and intensity, represented through the values of air  
 921 temperature at 850 hPa [K] exceeding the 90th percentile in the domain [0-40°N, 20°W-

922 20°E] [Lavaysse et al., 2009]. The SHL position and intensity is determined by detecting the  
923 maximum of the air temperature at 850 hPa inside the domain.

924



925

926

Figure 4: JJAS wind field at 700 hPa [m/s]: (left) climatological means for the CTL

927

simulation and the sensitivity experiments, and (right) differences between the sensitivity

928

experiments and the CTL simulation. In panel (h), the difference between the GSRD and

929

GSPD experiments is shown. Significance at 95% confidence level is displayed. Shadings

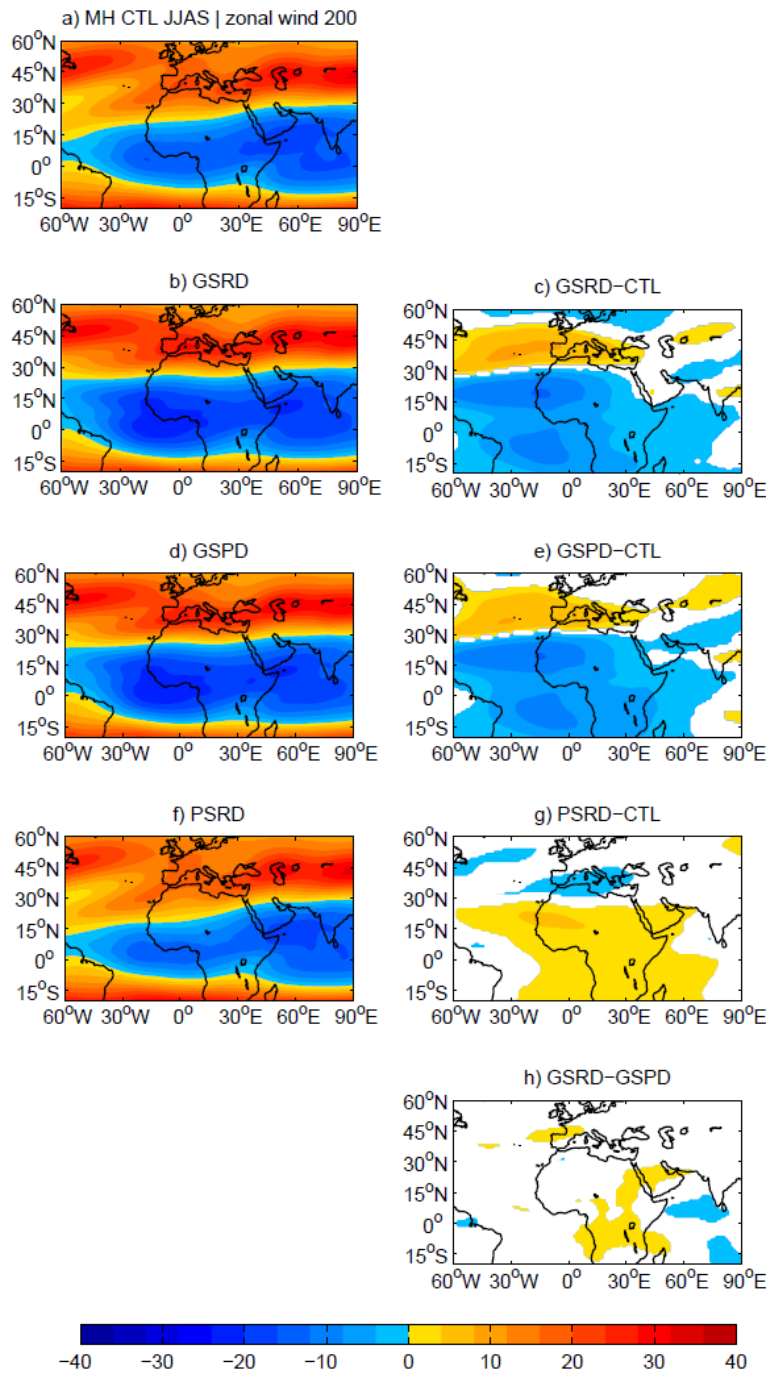
930

indicate the Saharan high location and intensity, represented through the geopotential height

931

at 700 hPa exceeding 3150 m. Red lines represent the mean positions of the African easterly

932 jet in the CTL simulation (dashed) and the sensitivity experiments (solid). The mean axis of  
933 the African easterly jet is determined in the domain [20°W-20°E, 0°-40°N] by detecting, at  
934 each longitude, the latitudinal location of the minimum of the zonal wind at 700 hPa, and  
935 averaging along the zonal direction.  
936

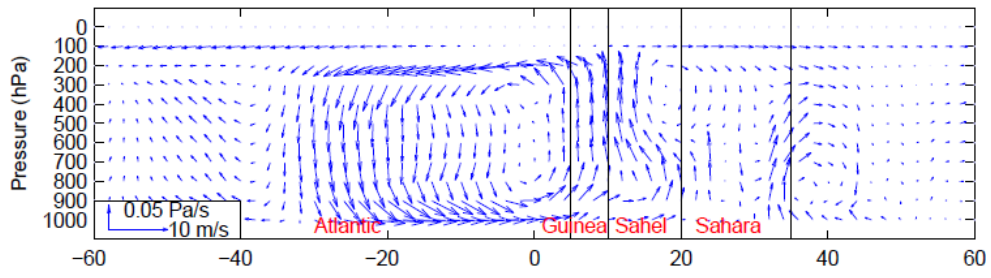


937

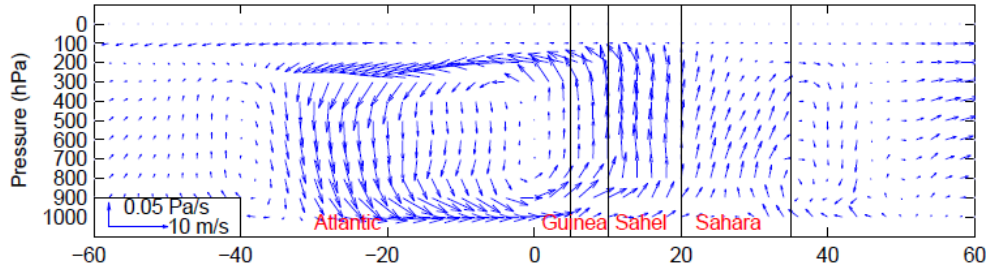
938 Figure 5: JJAS wind field at 200 hPa [m/s]: (left) climatological means for the CTL  
 939 simulation and the sensitivity experiments, and (right) differences between the sensitivity  
 940 experiments and the CTL simulation. In panel (h), the difference between the GSRD and  
 941 GSPD experiments is shown. Significance at 95% confidence level is displayed.

942

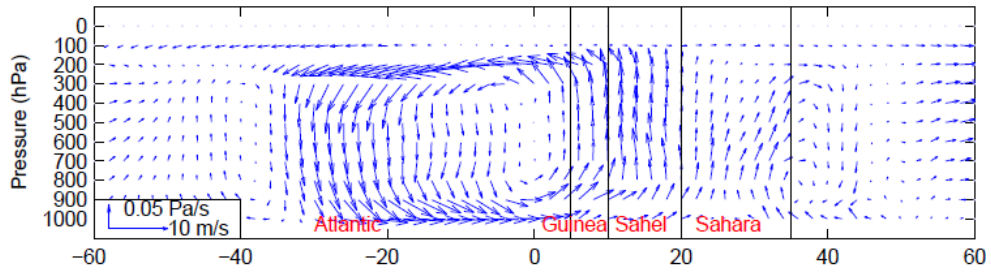
a) MH JJAS CTL ( $v, -\omega$ ) 10°W–10°E



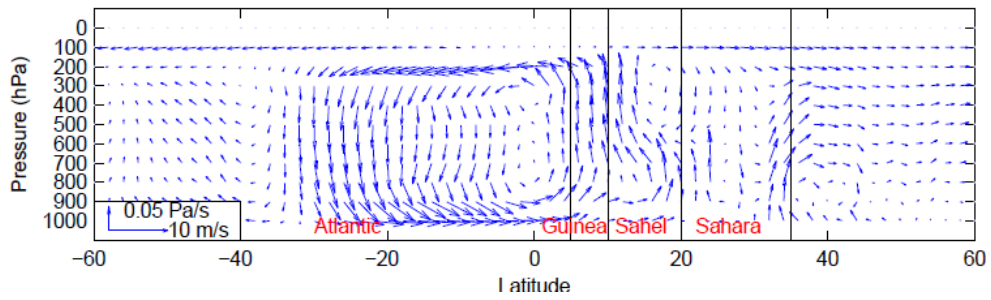
b) GSRD

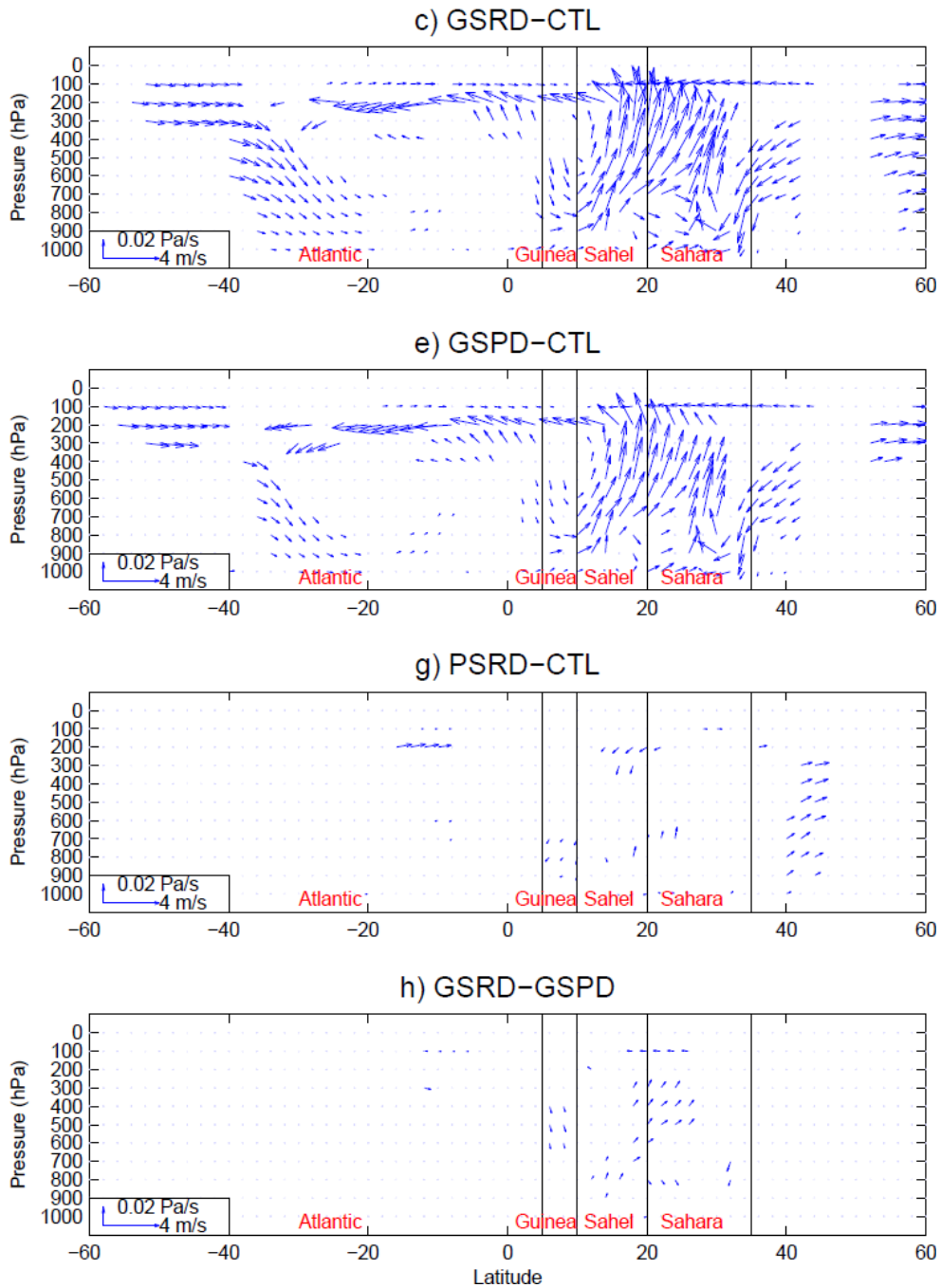


d) GSPD



f) PSRD





944

945 Figure 6: JJAS meridional overturning circulation, represented through the meridional wind

946 [m/s] and the vertical velocity [Pa/s], averaged in the range [10°W, 10°E]: (left)

947 climatological means for the CTL simulation and the sensitivity experiments, and (right)

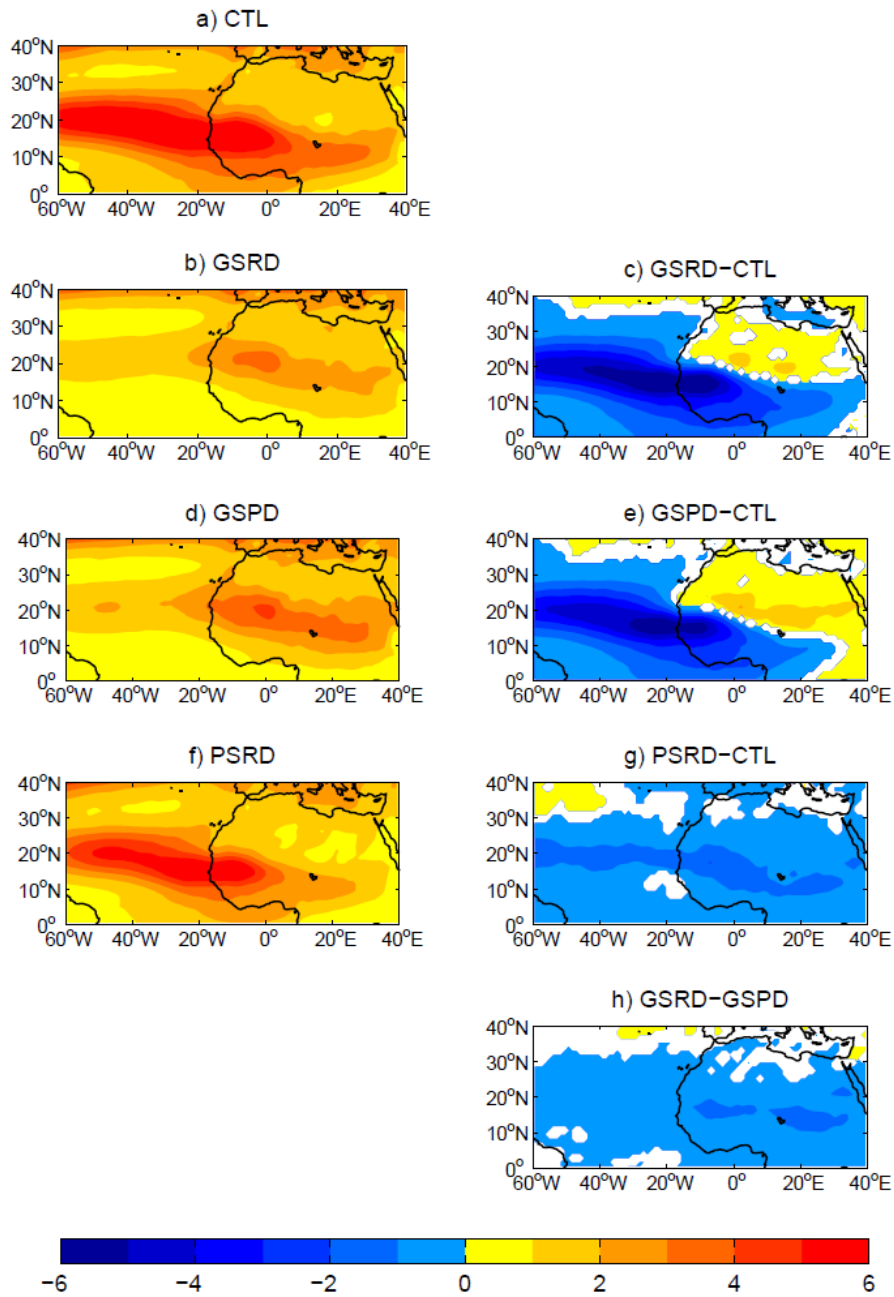
948 differences between the sensitivity experiments and the CTL simulation. In panel (h), the

949 difference between the GSRD and GSPD experiments is shown. Significance at 95%

950 confidence level is displayed.

951

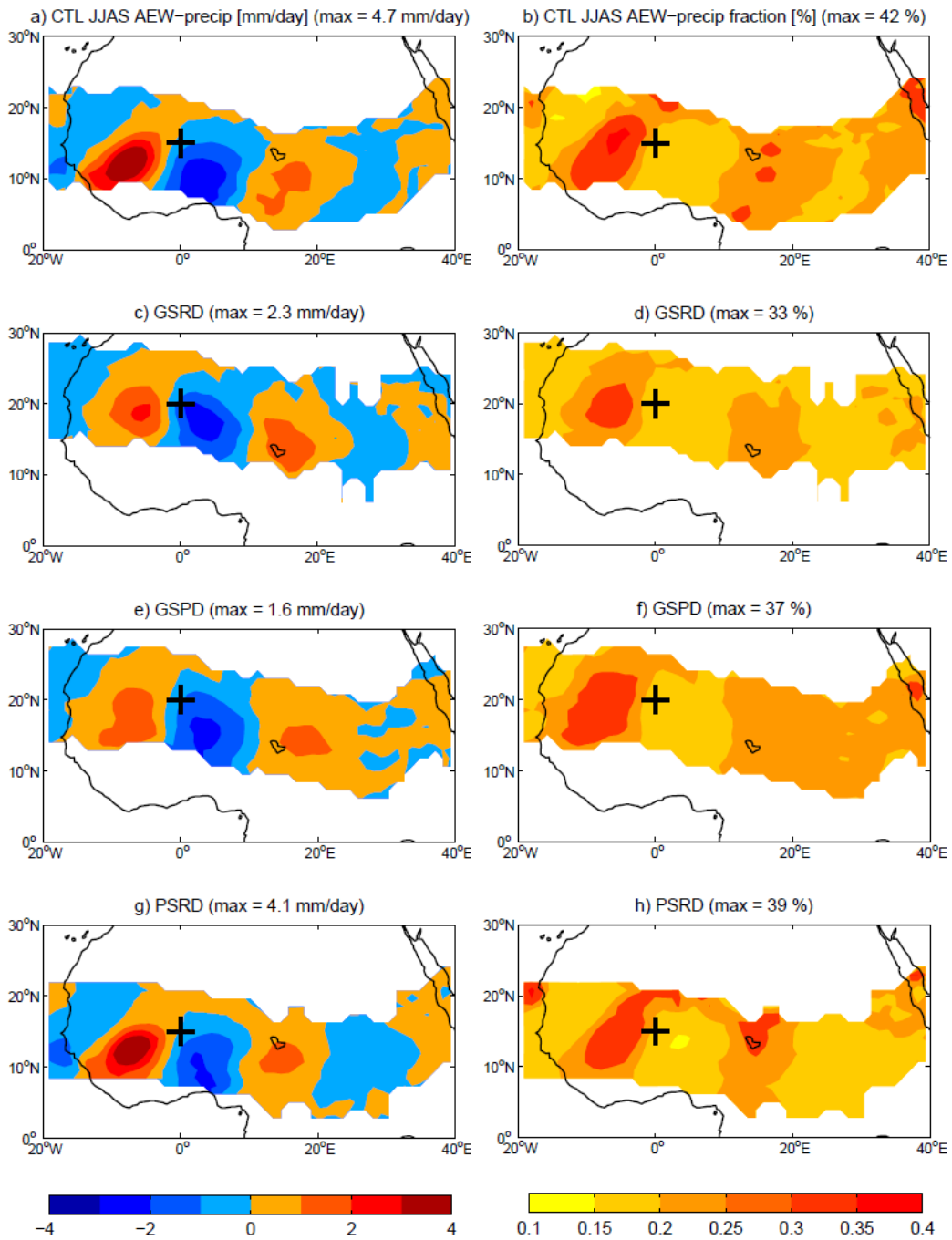
JJAS AEWs : variance of 700 hPa meridional wind (2.5–5-day filtered) [ $\text{m}^2/\text{s}^2$ ]



952

953 Figure 7: JJAS African easterly wave activity, represented through the variance of the  
 954 meridional wind at 700 hPa filtered in the 2.5-5-day band [ $\text{m}^2/\text{s}^2$ ]: (left) climatological means  
 955 for the CTL simulation and the sensitivity experiments, and (right) differences between the  
 956 sensitivity experiments and the CTL simulation. In panel (h), the difference between the  
 957 GSRD and GSPD experiments is shown. Significance at 95% confidence level is displayed,  
 958 computed by using a two-sample F test.

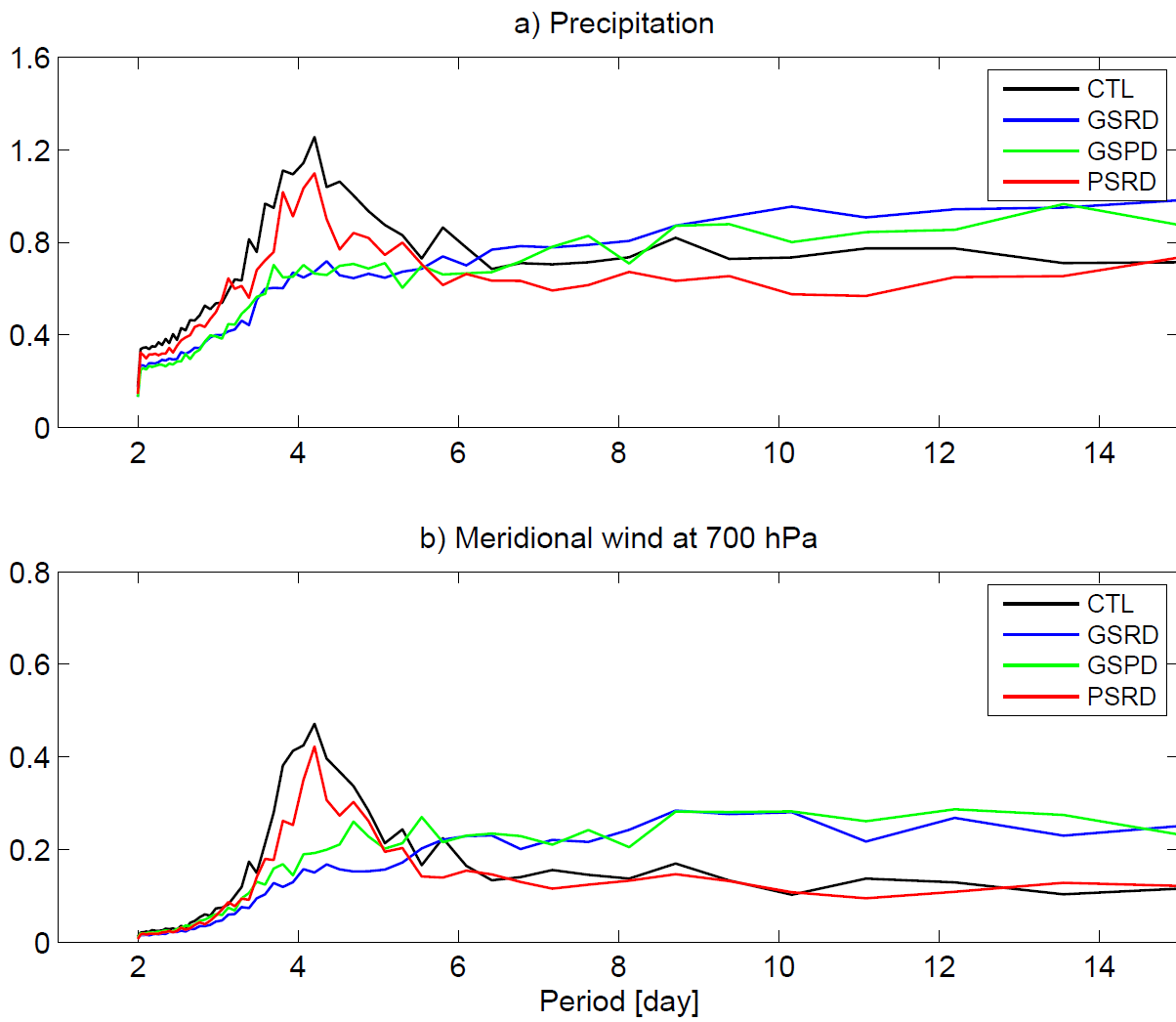
959



960

961 Figure 8: Precipitation associated with the African easterly waves detected in JJAS at  
 962 locations indicated by black crosses: (left) precipitation anomalies [mm/day] compared to the  
 963 JJAS climatology, and (right) fraction of the JJAS total precipitation. In brackets at the top of  
 964 each panel, values and fraction of the peak precipitation anomaly to the west of the black  
 965 crosses. Only values in a 15° latitudinal band around the maximum of the meridional wind  
 966 variance (see Figure 7) are displayed.

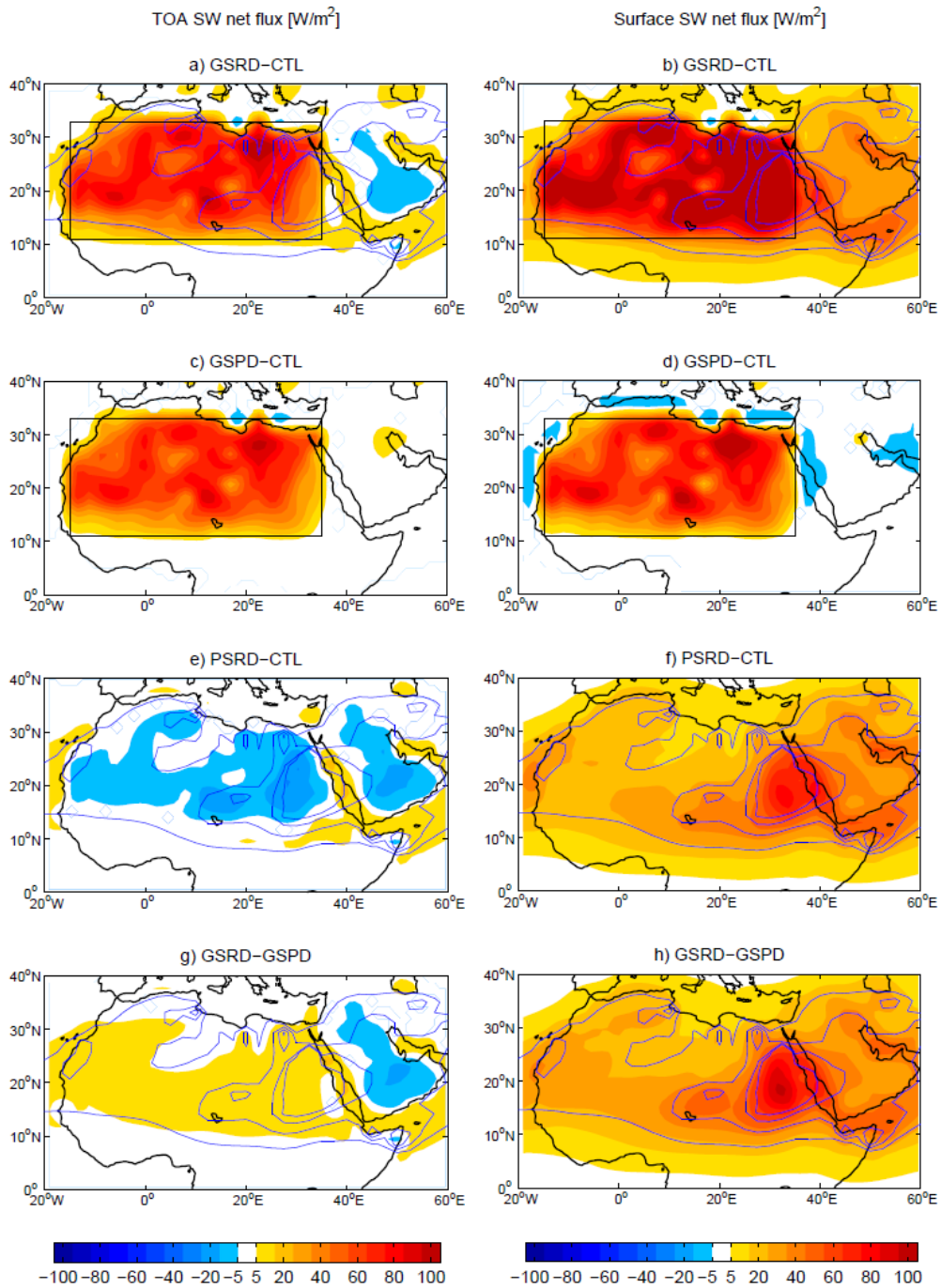
967



968

969 Figure 9: Fast Fourier transform analysis of grid-point JJAS daily (a) precipitation and (b)  
 970 meridional wind at 700 hPa, averaged over  $[5^{\circ}\text{-}16^{\circ}\text{N}, 10^{\circ}\text{W-}10^{\circ}\text{E}]$  for the CTL and PSRD  
 971 simulations and  $[5^{\circ}\text{-}28^{\circ}\text{N}, 10^{\circ}\text{W-}10^{\circ}\text{E}]$  for the GSRD and GSPD simulations.

972

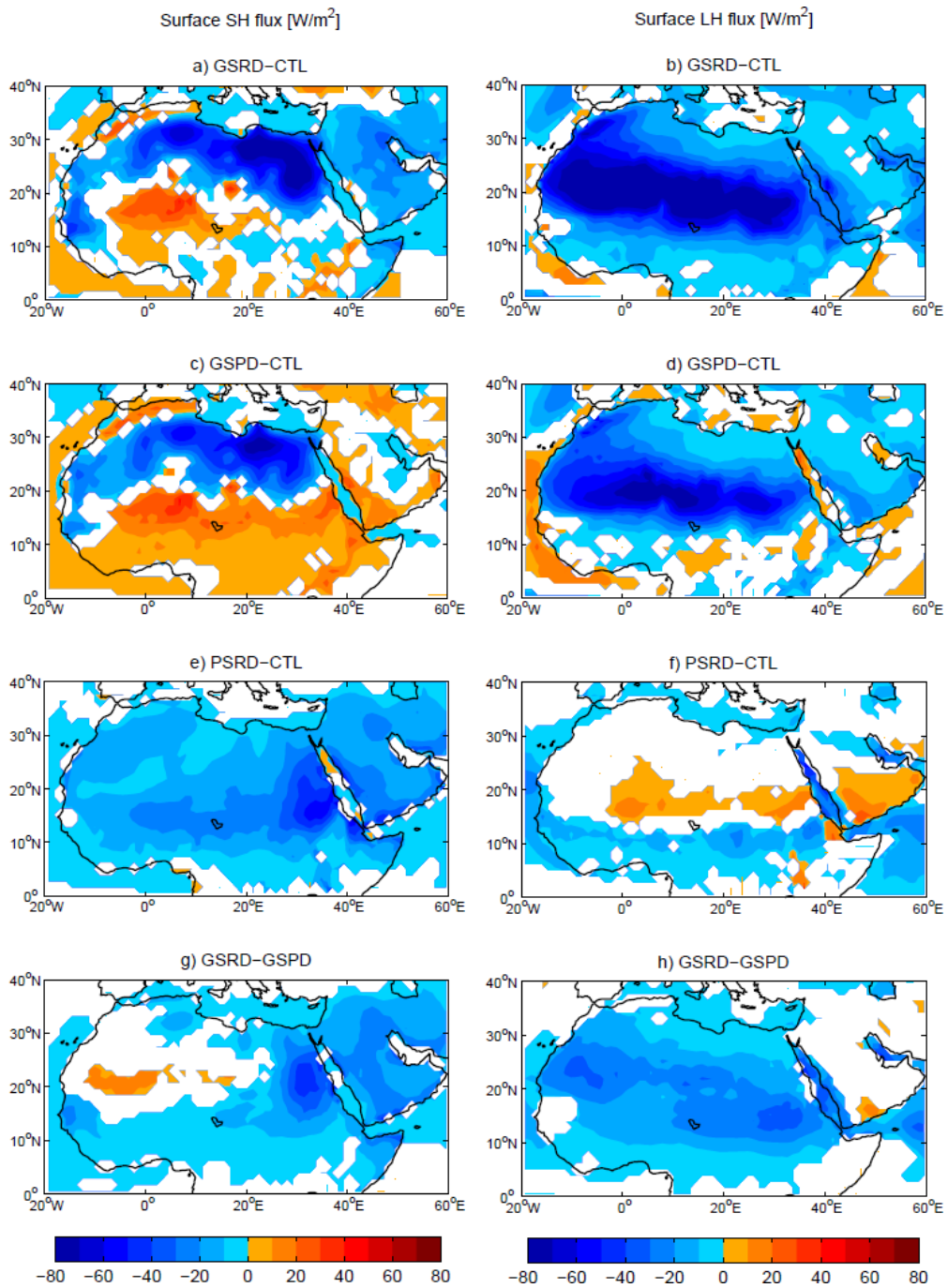


973

974 Figure 10: JJAS clear-sky SW radiation net flux [ $\text{W/m}^2$ ] at (left) TOA and (right) surface:  
 975 (1st-3rd row) differences between the sensitivity experiments and the CTL simulation, (4th  
 976 row) GSRD-GSPD difference. Significance at 95% confidence level is displayed. Radiation  
 977 is represented as 24-h means, positive values indicate downward net flux. The black rectangle  
 978 represents the domain where the change in land cover is applied in the Green Sahara

979 experiments. Blue contours display the dust column concentration anomaly in the reduced  
980 dust experiments (contours at -2, -1.5, -1, -0.5 mg/kg; see Figure 1b).

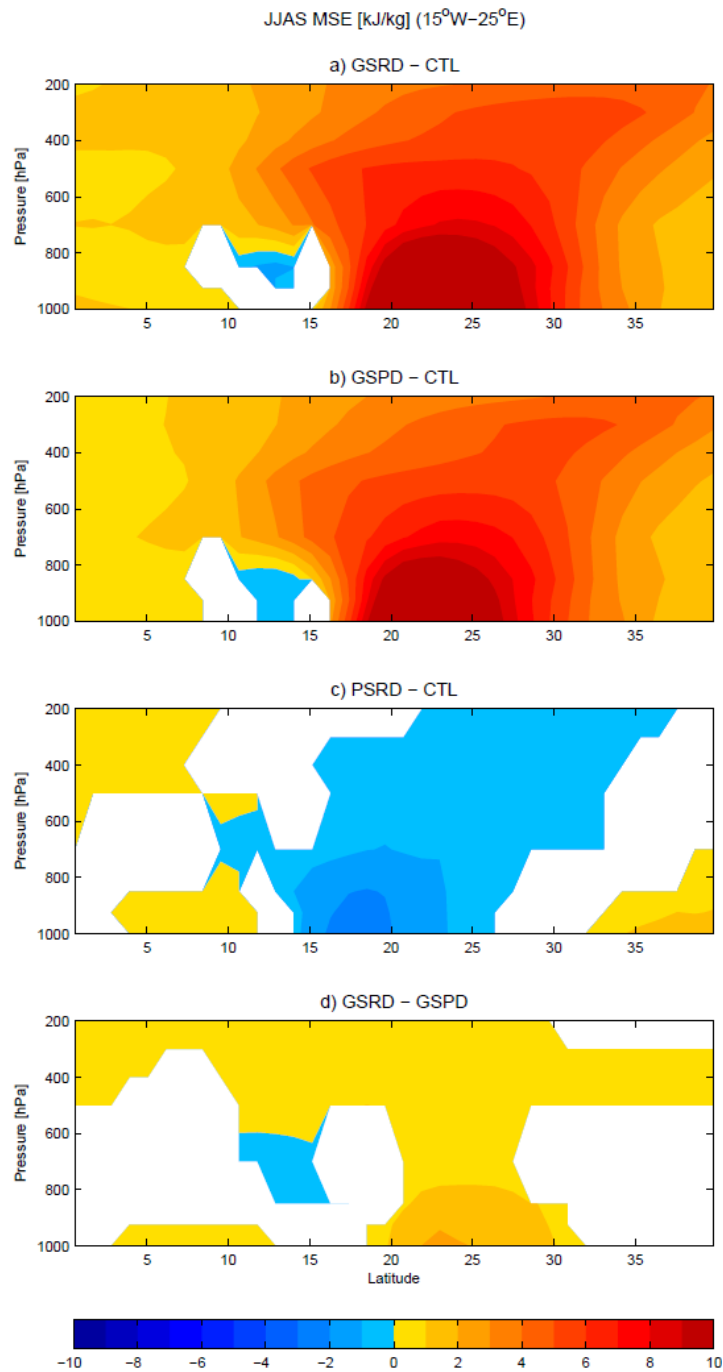
981



982

983 Figure 11: JJAS surface (left) sensible and (right) latent heat flux [ $\text{W/m}^2$ ]: (1st-3rd row)  
 984 differences between the sensitivity experiments and the CTL simulation, (4th row) GSRD-  
 985 GSPD difference. Significance at 95% confidence level is displayed. Positive values indicate  
 986 downward flux.

987



988

989 Figure 12: JJAS moist static energy [kJ/kg], averaged between  $15^{\circ}\text{W}$  and  $25^{\circ}\text{E}$ : (a-c)  
 990 differences between the sensitivity experiments and the CTL simulation are displayed in  
 991 panels, and (c) GSRD-GSPD difference. Significance at 95% confidence level is displayed.

992